A space–time discontinuous Galerkin method for linearized elastodynamics with element-wise momentum balance

R. Abedi [a], B. Petracovici [b,1], R.B. Haber [a,*]

[a] *Department of Theoretical and Applied Mechanics, University of Illinois at Urbana-Champaign,
104 South Wright St., Urbana, IL 61801, USA*
[b] *Department of Mathematics, Western Illinois University, 1 University Circle, Macomb, IL 61455, USA*

Abstract

We present a new space–time discontinuous Galerkin finite element method for linearized elastodynamics that delivers exact balance of linear and angular momentum over every space–time element. The method is formulated for use with fully unstructured space–time grids and uses displacement basis functions that are discontinuous across all inter-element boundaries. We introduce a new space–time formulation of continuum elastodynamics that uses differential forms and the exterior calculus on manifolds to generate a system of space–time field equations and jump conditions. Then we invoke a Bubnov–Galerkin weighted residuals procedure to formulate the finite element method. We describe an implementation on patch-wise causal meshes that features linear complexity in the number of elements and special per-pixel accurate visualization. Numerical examples confirm an a priori error estimate and demonstrate the method's shock-capturing capabilities.
© 2005 Elsevier B.V. All rights reserved.

Keywords: Discontinuous Galerkin; Spacetime; Finite element; Elastodynamics; Shocks

1. Introduction

1.1. Scope

This paper presents a new space–time discontinuous Galerkin finite element method for linearized elastodynamics. The method derives from a space–time formulation of the continuum problem in which

---

* Corresponding author.
 E-mail addresses: rabedi@uiuc.edu (R. Abedi), b-petracovici@wiu.edu (B. Petracovici), r-haber@uiuc.edu (R.B. Haber).
[1] Formerly, Department of Mathematics, University of Illinois at Urbana-Champaign.

continuity of the space–time displacement field is not assumed a priori. The formulation develops the continuum equations over an arbitrary space–time control volume, emphasizing the appropriate jump conditions for cases in which the solution is not smooth, as when material discontinuities or shocks are present.

The continuum space–time control volumes are associated with individual space–time elements in the finite element model, which uses a Bubnov–Galerkin weighted residuals procedure to develop the discrete discontinuous Galerkin equations. The resulting finite element method balances linear and angular momentum to within machine precision over every space–time element. It is dissipative, so no extra stabilization is required, although the numerical dissipation is relatively small in practice. These properties yield a method with excellent shock capturing capabilities. There are no spurious global oscillations when shocks are present; only a limited amount of non-polluting overshoot and undershoot in the immediate vicinity of propagating shock fronts.

Although the formulation can be used with any reasonable mesh partition of the space–time analysis domain, our implementation uses unstructured space–time meshes that satisfy a special causality constraint. This structure supports an interleaved mesh generation and solution procedure, in which small patches of space–time elements are solved as soon as they are generated. The resulting algorithm offers linear complexity in the number of elements (for any fixed polynomial order) and is rich in parallel structure. We also describe special per-pixel accurate visualization techniques that deliver high-definition renderings of solution data stored on unstructured space–time grids.

1.2. Related work

Semi-discrete conforming finite element methods are the most common numerical method for solving elastodynamics problems. In these methods, finite elements discretize the spatial domain, and weak enforcement of the equation of motion produces a system of ordinary differential equations in time (see, for example, [1]). These schemes tend to have one or more shortcomings, including failure to preserve the invariants of the mechanical system (e.g., energy or momentum) or an inability to capture shocks with sufficient accuracy. Shocks often excite spurious high-frequency oscillations in numerical solutions computed with these methods. Filtering or extra stabilization can be added to mitigate this problem, but these remedies tend to yield overly diffuse solutions. The quest for more effective methods that address these problems remains an active area of research.

Variational integrators are designed to preserve one or more of the invariants of the mechanical system. These methods begin with a spatial discretization, and use Hamilton's principle to advance the solution in time. A theorem by Ge and Marsden [2] states that time-stepping algorithms with fixed time steps cannot simultaneously preserve energy, momentum and the symplectic form. This leads to a division of variational integrators with fixed time steps into two groups: those that preserve energy and momentum, and those that preserve momentum and the variational symplectic form. Methods with algorithmic conservation of energy and momentum (including angular momentum) are presented in Betsch and Steinmann [3,4] and in Graham and Jelenić [5]. The introduction of nonuniform time steps provides a means to circumvent the theorem's restrictions. Thus, recent variational algorithms that are symplectic as well as momentum and energy preserving, but with nonuniform time steps, are developed in Kane et al. [6] and in Lew et al. [7,8]. Nonlinear iterations are required in the methods that simultaneously achieve energy and momentum conservation and preservation of the symplectic format.

Time-discontinuous Galerkin methods, first introduced by Hulbert and Hughes [9,10] represent another recent development. These methods discretize space and time simultaneously with space–time finite element grids. They use basis functions that are continuous in space, but admit discontinuities in time at discrete intervals. See also Li and Wiberg [11,12] for adaptive time discontinuous Galerkin schemes. The stability and convergence properties of semi-discrete and time-discontinuous Galerkin methods are analyzed in

French [13], Johnson [14] and Romero [15]. The introduction of discontinuities in time adds a degree of intrinsic stabilization to these methods.

Spacetime discontinuous Galerkin (*SDG*) *methods* represent another recent focus of numerical methods development. Similar to time-discontinuous Galerkin methods, SDG methods also directly discretize space–time with finite elements, but fully unstructured space–time meshes are supported and the basis functions admit discontinuities across all inter-element boundaries. Discretizations of space–time domains with inclined boundaries provides an intrinsic capability to track moving boundaries. The use of unstructured space–time meshes to fill these domains offers the possibility of circumventing the mesh distortion and the need for remeshing that occurs in most boundary-tracking methods. Richter [16] (single-field formulation) and Falk and Richter [17] (two-field formulation) propose SDG methods for the wave equation that use explicit (or causal) partitions of the space–time domain.

Yin et al. propose an SDG method for linear elastodynamics in [18,19] that is similar in many respects to [16]. Their approach weakly enforces the equation of motion as well as the space–time jump conditions for momentum balance and kinematic compatibility in an energetically consistent manner. When implemented on causal space–time grids, the method has linear complexity in the number of elements. This method produces high-quality solutions, especially in shock-capturing problems where no extra stabilization is required to suppress spurious global oscillations. However, this method is dissipative (so it does not balance energy), and it guarantees element-wise momentum balance only on a restrictive class of space–time meshes.

The method introduced in this paper addresses some of the drawbacks of the method presented in [18,19] while retaining its advantages. It guarantees exact element-wise momentum balance on any space–time grid by decoupling the weak enforcement of momentum balance from the control on the zero-energy subspace of steady, infinitesimal-rigid deformations. The method differs from previous formulations for elastodynamics in that, following ideas from Palaniappan et al. [20], the space–time jump conditions on the element boundaries are enforced relative to physically and mathematically consistent *target values*, rather than boundary traces from adjacent elements. The target values are either prescribed data on the domain boundary or Godunov values computed as solutions to local Riemann problems on the domain interior. The use of jump conditions based on target values provides a unified method for enforcing initial conditions and boundary conditions on the overall space–time domain as well as the necessary space–time jump conditions on interior inter-element boundaries. The use of Godunov target values delivers more accurate solutions than are obtained with averaged values, especially for problems with non-smooth solutions.

1.3. Organization of this paper

The remainder of this paper is organized as follows. Section 2 introduces a space–time formulation of continuum linearized elastodynamics using the mathematical machinery of differential forms and the exterior calculus on manifolds. Jump conditions, derived from the balance of linear momentum and from kinematic compatibility, play a central role in both the continuum formulation and in the subsequent development of the discontinuous Galerkin formulation. We use the Method of Weighted Residuals to develop the new space–time discontinuous Galerkin finite element formulation in Section 3; Section 4 summarizes the results of stability and error analyses from [21]. We describe certain aspects of our numerical implementation in Section 5, including the construction of causal space–time meshes with the Tent Pitcher algorithm [22,23], an advancing-front solution algorithm with linear complexity in the number of space–time elements, and special per-pixel accurate visualization methods for data stored on unstructured space–time grids. Numerical studies of convergence rates and an example simulation of shock propagation in a solid-fuel rocket grain appear in Section 6. Following concluding remarks in Section 7, we present component expansions of the finite element equations in Appendix A and the definitions of certain Godunov values in Appendix B.

2. Continuum formulation

We use differential forms and the exterior calculus on manifolds to develop a space–time continuum theory for linearized elastodynamics. This approach describes concisely the fundamental balance laws of mechanics as applied to arbitrary control volumes on a space–time manifold and, similarly to direct tensor notation in a purely spatial setting, helps to clarify the structure of our space–time continuum and discontinuous Galerkin finite element formulations.

Although our use of differential forms is nonstandard in mechanics, we believe that its advantages relative to conventional tensor notation support its use in the present space–time setting. For example, we obtain an invariant formulation that does not require the introduction of an extraneous space–time metric. The use of conventional tensor notation, on the other hand, requires the construction of space–time normal vectors, and this requires the introduction of an arbitrary scaling between space and time that precludes a coordinate-system-independent notation (see Appendix A). Applying our direct notation to space–time control volumes, we obtain a unified mathematical framework that addresses initial conditions, boundary conditions, and jump conditions on space–time surfaces with arbitrary orientations (see Section 2.6). This leads to a robust and modular software architecture that uses a single method to enforce all forms of initial, boundary and jump conditions in our finite element implementation.

2.1. Spacetime manifolds and notation for differential forms

Let d be the spatial dimension, and let the reference space–time analysis domain D be an open $(d+1)$-manifold in $\mathbb{E}^d \times \mathbb{R}$ with a regular boundary. The coordinates $(x^1, \ldots, x^d, t) = (\boldsymbol{x}, t)$ in D are defined with respect to the ordered basis $(\mathbf{e}_1, \ldots, \mathbf{e}_d, \mathbf{e}_t)$ and are understood to be material coordinates associated with the undeformed configuration of a body followed by the time coordinate. We follow the standard summation convention with Latin indices ranging from 1 through d, except the index 't' is reserved to indicate time and does not imply summation when repeated. The dual basis is denoted $(\mathbf{e}^1, \ldots, \mathbf{e}^d, \mathbf{e}^t)$. We introduce the $(d+1)$-vector $\mathbf{e}_{\boldsymbol{\Omega}} := \mathbf{e}_1 \wedge \cdots \wedge \mathbf{e}_d \wedge \mathbf{e}_t$ and define the d-vectors $\hat{\mathbf{e}}^t$ and $\hat{\mathbf{e}}^i$ via the relations $\mathbf{e}_t \wedge \hat{\mathbf{e}}^t = \mathbf{e}_{\boldsymbol{\Omega}}$ and $\mathbf{e}_i \wedge \hat{\mathbf{e}}^j = \delta_i^j \mathbf{e}_{\boldsymbol{\Omega}}$.

The standard basis for top forms on D is $\boldsymbol{\Omega} = \mathbf{d}x^1 \wedge \cdots \wedge \mathbf{d}x^d \wedge \mathbf{d}t$, and the d-form $\mathbf{d}\hat{x}_j$ is defined by $\mathbf{d}x^j \wedge \mathbf{d}\hat{x}_k = \delta_k^j \boldsymbol{\Omega}$; $\mathbf{d}t \wedge \mathbf{d}\hat{x}_k = \mathbf{0}$. We define the *temporal Lie derivative* as $\mathscr{L} := \mathscr{L}_{\bar{\mathbf{e}}_t}$ and the *temporal insertion* as $\mathbf{i} := \mathbf{i}_{\bar{\mathbf{e}}_t}$ in which $\bar{\mathbf{e}}_t$ is a vector field on D with uniform value $\mathbf{e}_t$. Thus, $\mathbf{d}t \wedge \mathbf{i}\boldsymbol{\Omega} = \boldsymbol{\Omega}$.

Let Γ be an orientable d-manifold in $\mathbb{E}^d \times \mathbb{R}$, and let $\{\mathbf{a}_1, \ldots, \mathbf{a}_d\}$ be an ordered basis for $T\Gamma$, the union of all tangent spaces to Γ, in which $\mathbf{a}_i$ is a vector field on Γ. The volume vector field for Γ corresponding to the basis $\{\mathbf{a}_i\}$ is the d-vector field given by

$$\mathbf{a}_\Gamma = \mathbf{a}_1 \wedge \cdots \wedge \mathbf{a}_d = a^i \hat{\mathbf{e}}_i + a^t \hat{\mathbf{e}}_t = \mathbf{a}_{\mathbf{x}} + \mathbf{a}_t. \tag{1}$$

The d-manifold Γ is either *vertical* if $\mathbf{i}\boldsymbol{\Omega}(\mathbf{a}_\Gamma) = 0 \iff a^t = 0$, or *inclined* if $\mathbf{i}\boldsymbol{\Omega}(\mathbf{a}_\Gamma) \neq 0 \iff a^t \neq 0$.

We use forms with vector as well as scalar coefficients to develop the theory, and we define the wedge product of two vector-valued forms as the form with scalar coefficients given by

$$(\mathbf{a} \otimes \boldsymbol{\psi}) \wedge (\mathbf{b} \otimes \boldsymbol{\omega}) = (\mathbf{a} \cdot \mathbf{b}) \boldsymbol{\psi} \wedge \boldsymbol{\omega}, \tag{2}$$

in which $\mathbf{a}$, $\mathbf{b}$ are vector fields in $\mathbb{E}^d(D)$ and $\boldsymbol{\psi}$, $\boldsymbol{\omega}$ are forms on D. Otherwise, we follow standard notation; the reader is referred to [24–26] for more complete expositions of differential forms and tensor calculus on manifolds.

2.2. Mechanical fields

2.2.1. Kinematics

The *displacement field* $\mathbf{u} : D \to \mathbb{E}^d$ has the component representation $\mathbf{u} = u_i \mathbf{e}^i$. The *strain-velocity* $\boldsymbol{\varepsilon}$ is the 1-form with vector coefficients given by

$$\boldsymbol{\varepsilon} := \mathbf{E} + \mathbf{v}, \tag{3}$$

in which $\mathbf{v} := \dot{\mathbf{u}} \otimes \mathbf{d}t = \dot{u}_i \mathbf{e}^i \otimes \mathbf{d}t$ is the *velocity*, and the *linearized strain* $\mathbf{E}$ has the component representation, $\mathbf{E} = E_{ij} \mathbf{e}^i \otimes \mathbf{d}x^j$, where $E_{ij} = \frac{1}{2}(u_{i,j} + u_{j,i})$.

We introduce the space of admissible displacement fields,

$$V(D) = \{ \mathbf{w} : \exists \mathscr{P}(D) = \{Q_\alpha\} \ni \mathbf{w}|_{Q_\alpha} \in H^2(Q_\alpha, \mathbb{E}^d) \},$$

in which $\mathbf{w} : D \to \mathbb{E}^d$ and $\mathscr{P}(D)$ is a partition of D into open subdomains Q_α with regular boundaries. $V(D)$ is a broken Sobolev space that admits discontinuous displacement fields. For any $Q \subset D$, let $V^Q := V(D)|_Q$. The *zero-energy subspace of* V^Q is given by $V_0^Q := \{ \mathbf{w} \in V^Q : \boldsymbol{\varepsilon}(\mathbf{w}) = 0 \}$. V_0^Q contains all time-independent, infinitesimal-rigid displacement fields $\mathbf{w}$ of the form

$$\mathbf{w}(\mathbf{x}) = \mathbf{c} + \mathbf{S}x, \quad \forall \mathbf{x} = (x,t) \in Q, \tag{4}$$

in which $\mathbf{c} \in \mathbb{E}^d$ and $\mathbf{S}$ is a skew-symmetric tensor on $\mathbb{E}^d$.

We define the *temporal inflow boundary* of Q as $\partial Q^{\mathrm{ti}} := \{ \mathbf{x} \in \partial Q : \mathbf{i}\boldsymbol{\Omega}(\mathbf{a}_{\partial Q}(\mathbf{x})) < 0 \}$ in which $\mathbf{a}_{\partial Q}$ is the volume vector field on the d-manifold ∂Q. V^Q admits the decomposition $V^Q = V_0^Q \oplus V_\varepsilon^Q$ with respect to the inner product $\langle\langle \mathbf{w}, \mathbf{v} \rangle\rangle_Q := \langle \mathbf{w}, \mathbf{v} \rangle_{\partial Q^{\mathrm{ti}}} + \int_Q \boldsymbol{\varepsilon}(\mathbf{w}) \wedge \mathbf{C}\boldsymbol{\varepsilon}(\mathbf{v})$ where $\langle \mathbf{w}, \mathbf{v} \rangle_{\partial Q^{\mathrm{ti}}} := -\int_{\partial Q^{\mathrm{ti}}} (\mathbf{w} \cdot \mathbf{v}) \mathbf{i}\boldsymbol{\Omega}$ and $\mathbf{C}$ is a positive-definite linear transformation of vector-valued 1-forms into vector-valued d-forms, specifically, the constitutive map defined in Section 2.5. Thus, given any $\mathbf{u} \in V^Q$, we have the unique decomposition $\mathbf{u} = \mathbf{u}_0 + \mathbf{u}_\varepsilon$ in which $\mathbf{u}_0 \in V_0^Q$ and $\mathbf{u}_\varepsilon \in V_\varepsilon^Q$.

2.2.2. Force-like fields

The *stress* $\boldsymbol{\sigma}$ is the d-form with vector coefficients defined by $\mathbf{t}_\Gamma = \boldsymbol{\sigma}\mathbf{a}_\Gamma$, in which $\mathbf{t}_\Gamma$ is the surface traction field acting on a d-manifold $\Gamma \subset D$, and $\mathbf{a}_\Gamma$ is the volume vector field for Γ, as defined in (1). The component representation of $\boldsymbol{\sigma}$ is given by

$$\boldsymbol{\sigma} = \sigma^{ij} \mathbf{e}_i \otimes \mathbf{d}\hat{x}_j. \tag{5}$$

The *linear momentum density* $\mathbf{p}$ is the d-form with vector coefficients defined by $\mathbf{p}\hat{\mathbf{e}}^t = \bar{\mathbf{p}}$, in which $\bar{\mathbf{p}} : D \to \mathbb{E}^d$ is the linear momentum measured per unit volume in the reference configuration. The component representation of $\mathbf{p}$ is given by

$$\mathbf{p} = p^i \mathbf{e}_i \otimes \mathbf{i}\boldsymbol{\Omega}. \tag{6}$$

We combine the stress and the linear momentum density to form the *space–time flux of linear momentum*[2]

$$\mathbf{M} = \boldsymbol{\sigma} - \mathbf{p}. \tag{7}$$

The *body force density* $\mathbf{b}$ is the $(d+1)$-form with vector coefficients such that $\mathbf{b}\mathbf{e}_Q = \bar{\mathbf{b}}$, where $\bar{\mathbf{b}} : D \to \mathbb{E}^d$ is the vector field that delivers body force per unit mass on D. The component representation of $\mathbf{b}$ is given by

$$\mathbf{b} = b^i \mathbf{e}_i \otimes \boldsymbol{\Omega}. \tag{8}$$

---

[2] In 1972, Gurtin introduced a '*four-tensor* field with space–time partition' called the *stress-momentum field* that is similar in concept to our space–time flux of linear momentum. See [27, pp. 67, 253].

2.2.3. Energy density

The *total energy density* $\mathbf{\Phi} = \Phi\mathbf{\Omega}$ is the non-negative $(d+1)$-form with scalar coefficients such that $\mathbf{\Phi}\mathbf{e}_\Omega = \Phi = K + U$, in which $\Phi : D \to \mathbb{R}$ is the sum of the *kinetic energy density* K and the *internal energy density* U, each measured per unit volume in the undeformed configuration. The functions describing K and U are defined in the section on the constitutive model below.

2.3. Kinematic compatibility

Kinematic compatibility requires that for any d-manifold $\Gamma \subset D$,

$$(\mathbf{u}^+ - \mathbf{u}^-)|_\Gamma = \mathbf{0}, \tag{9}$$

where $\mathbf{u}^\pm$ are limiting values of $\mathbf{u}$ on opposing sides of Γ. Next, we introduce subdomain-based jump conditions that serve in lieu of (9).

The following system enforces the jump condition (9) and also sets the value of $\mathbf{u}|_\Gamma$ equal to a physically consistent target value $\mathbf{u}^*$ on all $\Gamma \subset D$.[3] For all $Q \subset D$,

$$(\boldsymbol{\varepsilon}^* - \boldsymbol{\varepsilon})|_{\partial Q} = \mathbf{0}, \tag{10a}$$

$$(\mathbf{u}_0^* - \mathbf{u}_0)|_{\partial Q^{\mathrm{ti}}} = \mathbf{0}, \tag{10b}$$

in which

$$\mathbf{u}_0 = \sum_\alpha \langle\langle \mathbf{w}_\alpha, \mathbf{u} \rangle\rangle_Q \mathbf{w}_\alpha = \sum_\alpha \langle \mathbf{w}_\alpha, \mathbf{u} \rangle_{\partial Q^{\mathrm{ti}}} \mathbf{w}_\alpha, \tag{11a}$$

$$\mathbf{u}_0^* = \sum_\alpha \langle \mathbf{w}_\alpha, \mathbf{u}^* \rangle_{\partial Q^{\mathrm{ti}}} \mathbf{w}_\alpha, \tag{11b}$$

where $\mathbf{u} \in V^Q$, $\mathbf{u}^*$ is the target displacement field on ∂Q^{ti} and $\{\mathbf{w}_\alpha\}$ is an orthonormal basis for V_0^Q. The term $\boldsymbol{\varepsilon}^*$ denotes a target strain-velocity field on ∂Q that is determined by suitable Riemann problems or by prescribed initial and boundary data on certain parts of ∂D. Thus, system (10) enforces kinematic compatibility on the interior of D as well as the kinematic boundary and initial conditions. Specific expressions for the target values are provided in Section 2.6 and in Appendix B.

2.4. Balance laws

2.4.1. Momentum balance
Balance of linear momentum requires that

$$\int_{\partial Q} \mathbf{M} + \int_Q \rho\mathbf{b} = 0, \quad \forall Q \subset D. \tag{12}$$

The following system enforces system (12) via the Stokes theorem, while enforcing target fluxes $\mathbf{M}^*$ on ∂Q that are consistent with Riemann solutions or prescribed initial and boundary data. Specific expressions for $\mathbf{M}^*$ appear in Section 2.6 and Appendix B.

For all $Q \subset D$,

$$(\mathbf{dM} + \rho\mathbf{b})|_{Q \setminus \Gamma^J} = \mathbf{0}, \tag{13a}$$

$$(\mathbf{M}^* - \mathbf{M})|_{\partial Q \cup (Q \cap \Gamma^J)} = \mathbf{0}, \tag{13b}$$

where Γ^J is the jump set of $\mathbf{M}$ on Q.

---

[3] See [21] for a proof that system (10) implies (9).

If balance of linear momentum is satisfied, then *balance of angular momentum* is equivalent to the condition that for any infinitesimal-rigid rotation $\mathbf{S}x \in V_0$ (cf. (4)),

$$\int_{\partial Q} \mathbf{S}x \wedge \mathbf{M} + \int_Q \mathbf{S}x \wedge \rho\mathbf{b} = 0, \quad \forall Q \subset D. \tag{14}$$

Alternatively, if balance of linear momentum is satisfied, then symmetry of $\boldsymbol{\sigma}$

$$\sigma^{ij} = \sigma^{ji} \tag{15}$$

is equivalent to balance of angular momentum. From here on, we assume that (15) is satisfied, so that balance of linear momentum implies balance of angular momentum.

Remark 1. The component form of (13a) is $[\sigma^{ij}_{,j} + \rho(b^i - \ddot{u}^i)]\mathbf{e}_i \otimes \boldsymbol{\Omega} = \mathbf{0}$ on $Q \backslash \Gamma^J$. Thus, (13a) is the familiar *equation of motion*.

2.4.2. Energy balance

The *space–time flux of total energy* $\mathbf{N}$ is the d-form

$$\mathbf{N} := -\mathbf{i}\boldsymbol{\Phi} + \dot{\mathbf{u}} \wedge \boldsymbol{\sigma}. \tag{16}$$

Balance of energy requires that

$$\int_{\partial Q} \mathbf{N} + \int_Q \dot{\mathbf{u}} \wedge \rho\mathbf{b} = 0, \quad \forall Q \subset D. \tag{17}$$

2.5. Constitutive model

We restrict our attention to materials with linear elastodynamic response. That is, we assume the existence of a *space–time total energy density function* $\boldsymbol{\Phi}(\boldsymbol{\varepsilon})$ of the form,

$$\boldsymbol{\Phi} = \frac{1}{2}\boldsymbol{\varepsilon} \wedge \mathbf{C}\boldsymbol{\varepsilon}, \tag{18}$$

in which $\boldsymbol{\Phi}$ is a non-negative $(d+1)$-form with scalar coefficients such that

$$\frac{\partial \boldsymbol{\Phi}}{\partial \mathbf{E}} = \boldsymbol{\sigma}, \qquad \frac{\partial \boldsymbol{\Phi}}{\partial \mathbf{v}} = \mathbf{p}. \tag{19}$$

Here $\mathbf{C}$ is a positive-definite linear transformation of 1-forms with vector coefficients into d-forms with vector coefficients, that delivers

$$\mathbf{C}\boldsymbol{\varepsilon} = \boldsymbol{\sigma} + \mathbf{p}, \tag{20a}$$

$$\mathbf{p} = \mathbf{C}\mathbf{v}, \qquad \text{where } p^i = \rho\delta^{ij}\dot{u}_j, \tag{20b}$$

$$\boldsymbol{\sigma} = \mathbf{C}\mathbf{E}, \qquad \text{where } \sigma^{ij} = C^{ijkl}E_{kl}, \tag{20c}$$

in which ρ is the mass density per unit volume in the reference configuration, δ is the Kronecker delta, and C^{ijkl} are components of the familiar elasticity tensor that exhibit the usual major and minor symmetries: $C^{ijkl} = C^{klij} = C^{jikl} = C^{ijlk}$. The minor symmetry involving indices i and j enforces symmetry of $\boldsymbol{\sigma}$, cf. (15). In the case of an isotropic material, the elasticity components are given by

$$C^{ijkl} = \lambda\delta^{ij}\delta^{kl} + \mu(\delta^{ik}\delta^{jl} + \delta^{il}\delta^{jk}), \tag{21}$$

where λ and μ are the Lamé parameters. The positive-definite property of $\mathbf{C}$ means that there exists a positive constant k, such that

$$(\boldsymbol{\alpha} \wedge \mathbf{C}\boldsymbol{\alpha})\mathbf{e}_{\Omega} > k|\boldsymbol{\alpha}|^2 \tag{22}$$

for all 1-forms $\boldsymbol{\alpha}$ with vector coefficients.

For any linear transformation $\mathbf{C}$ as described in (18)–(22), there is a related linear transformation $\widehat{\mathbf{C}}$, that maps strain-velocity into momentum flux, according to

$$\mathbf{M} = \widehat{\mathbf{C}}\boldsymbol{\varepsilon} := \mathbf{C}(\mathbf{E} - \mathbf{v}). \tag{23}$$

In the present case of linear elasticity, it can be shown that the space–time flux of the total energy takes the form

$$\mathbf{N} = \frac{1}{2}(\mathbf{i}\boldsymbol{\varepsilon} \wedge \mathbf{M} + \boldsymbol{\varepsilon} \wedge \mathbf{i}\mathbf{M}). \tag{24}$$

2.6. Boundary partitions and specification of boundary target values

The jump conditions (10a), (10b) and (13b) require the evaluation of prescribed data and Godunov values, collectively called target values and denoted by a superscript "$*$", on the boundary of each subdomain Q of D. These values are determined by prescribed boundary data or the principle of causality as information propagates in space–time along the characteristic directions of the elastodynamic equations. Causality induces two partitions of ∂Q as described below. The first partition is used to specify $\mathbf{u}^*$, while the second is used to specify $\boldsymbol{\varepsilon}^*$ and $\mathbf{M}^*$.

2.6.1. Temporal partition of ∂Q and specification of $\boldsymbol{u}^*$

The temporal partition of ∂Q arises from causal relations that take the form of rate equations with characteristics in the $\mathbf{e}_t$ direction. These characteristics partition ∂Q into the *temporal inflow boundary* ∂Q^{ti} (cf. 2.2.1) and its complement, the *temporal outflow boundary* ∂Q^{to} (see Fig. 1a).

The target value $\mathbf{u}^*$ in (10b) is controlled by characteristics of the equation $\dot{u}_0 = 0$ in the $\mathbf{e}_t$ direction, and is, therefore, always determined by the earlier displacement value on ∂Q^{ti}. In particular, we have

$$\mathbf{u}^* = \begin{cases} \mathbf{u}^+ & \text{on } \partial Q^{\mathrm{ti}} \setminus \partial D^{\mathrm{ti}}, \\ \underline{\mathbf{u}} & \text{on } \partial Q^{\mathrm{ti}} \cap \partial D^{\mathrm{ti}}, \end{cases} \tag{25}$$

in which $\mathbf{u}^+$ is the exterior trace of $\mathbf{u}$ on ∂Q^{ti} and $\underline{\mathbf{u}}$ is the prescribed initial displacement field on ∂D^{ti}.
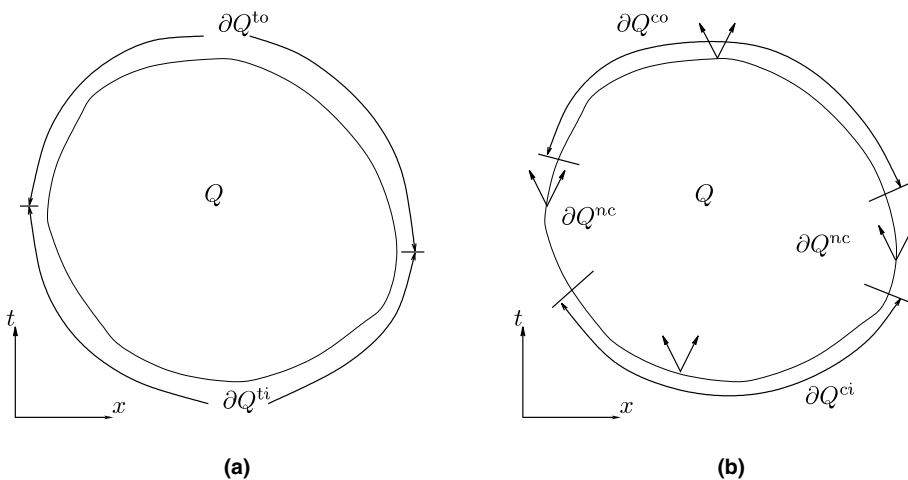
Fig. 1. Alternative partitions of ∂Q: (a) temporal partition, (b) causal partition.

2.6.2. Causal partition of ∂Q and specification of $\boldsymbol{\varepsilon}^*$ and $\boldsymbol{M}^*$

The second partition of ∂Q arises from characteristics associated with elastic wave propagation (see Fig. 1b). Information propagates within an elastic medium in a given spatial direction at finite speeds that are bounded by $c(\mathbf{n})$, the fastest wave speed in the spatial direction indicated by the unit vector $\mathbf{n} \in \mathbb{E}^d$. For a linearly elastic material,

$$c(\mathbf{n}) = \left(\frac{1}{\rho} \sup_{|\alpha|=1} C^{ijkl} \alpha_i \alpha_k n_j n_l \right)^{1/2}. \tag{26}$$

If the material is isotropic, then

$$c(\mathbf{n}) = c_p = \sqrt{\frac{\lambda + 2\mu}{\rho}}, \tag{27}$$

in which c_p is the pressure wave speed.

Let Γ be an orientable d-manifold in $\mathbb{E}^d \times \mathbb{R}$ with the volume vector field $\mathbf{a}_\Gamma$, as described in (1). We say that $(\boldsymbol{x}_0, t_0) \in \Gamma$ is a *causal point* with respect to Γ if

$$\left. \left(|a^t| - c(\mathbf{n}_0)|\mathbf{a}_x| \right) \right|_{(\boldsymbol{x}_0, t_0)} > 0, \tag{28}$$

in which $\mathbf{n}_0$ is the spatial unit normal to Γ at $(\boldsymbol{x}_0, t_0)$. A d-manifold is called *causal* if and only if all its points are causal points; a d-manifold that is not causal is called *noncausal* (see Fig. 2).

We partition ∂Q into its causal and noncausal parts, ∂Q^c and ∂Q^{nc}. We further partition ∂Q^c into its inflow and outflow parts: $\partial Q^c = \partial Q^{ci} \cup \partial Q^{co}$. All of the characteristics associated with elastic waves point inward to Q on the *causal inflow boundary* ∂Q^{ci}, while all characteristics point outward on the *causal outflow boundary* ∂Q^{co}. There are both inward and outward pointing characteristics on the *noncausal boundary* ∂Q^{nc} (see Fig. 1b).

Fig. 2 illustrates the significance of the causal property of a d-manifold $\Gamma_{\alpha\beta} = \partial Q_\alpha \cap \partial Q_\beta$. If $\Gamma_{\alpha\beta}$ is causal, then the information in the adjacent subdomain Q_β controls the solution in Q_α, but the solution in Q_β is independent of the solution in Q_α. In this case, we can compute the solution in Q_β before we compute the solution in Q_α. On the other hand, if $\Gamma_{\alpha\beta}$ is noncausal, the solutions in Q_α and Q_β are mutually dependent and, therefore, must be computed simultaneously. In the next section, we use the asymmetric dependency property of causal manifolds to develop a finite element procedure whose complexity scales linearly with the number of elements (for fixed polynomial order).

Initial and boundary data for $\boldsymbol{\varepsilon}$ and $\mathbf{M}$ are required on certain parts of ∂D to close the problem. Inflow data are required for both fields on ∂D^{ci}, while no data are specified on ∂D^{co}. There are many ways to
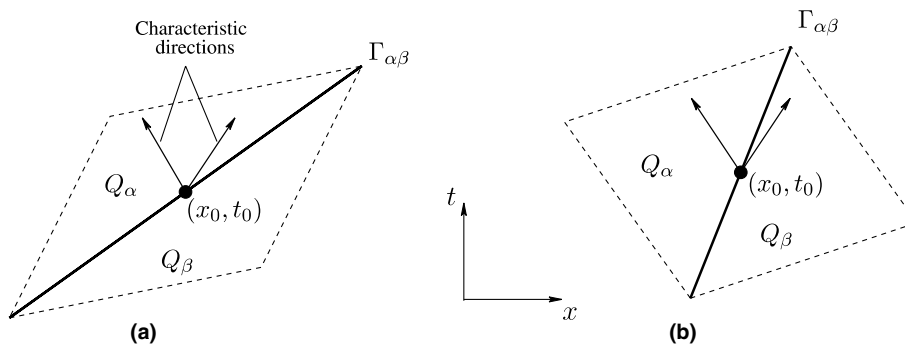

Fig. 2. Classification of manifolds based on causality: (a) causal manifold, (b) noncausal manifold.

specify physical boundary conditions for $\mathbf{M}$ and $\boldsymbol{\varepsilon}$ on the noncausal domain boundary ∂D^{nc}, and the number of terms that can be prescribed depends on the local configuration of ∂D relative to the characteristic surfaces for elastic wave propagation. To simplify matters, we restrict our attention to analysis domains where all of the noncausal parts of ∂D are vertical. We also assume a partition of the noncausal boundary into two regions where either $\mathbf{M}$ or $\boldsymbol{\varepsilon}$ is prescribed: $\partial D^{\mathrm{nc}} = \overline{\partial D^{\mathbf{M}} \cup \partial D^{\boldsymbol{\varepsilon}}}$. We obtain the *pure Dirichlet problem* when $\partial D^{\mathbf{M}} = \emptyset$ and the *pure Neumann problem* when $\partial D^{\boldsymbol{\varepsilon}} = \emptyset$. Otherwise, we have the *mixed problem*. We denote by $\underline{\mathbf{M}}$ the prescribed momentum flux field on $\partial D^{\mathrm{ci}} \cup \partial D^{\mathbf{M}}$ and by $\underline{\boldsymbol{\varepsilon}}$ the prescribed strain-velocity field on $\partial D^{\mathrm{ci}} \cup \partial D^{\boldsymbol{\varepsilon}}$.

We treat the jump conditions on the interior of D, the initial conditions and the boundary conditions in a unified fashion by specifying appropriate target values, $\mathbf{M}^*$ and $\boldsymbol{\varepsilon}^*$, as follows.

$$
\mathbf{M}^* = \begin{cases}
\mathbf{M} & \text{on } \partial Q^{\mathrm{co}} \cup (\partial Q \cap \partial D^{\boldsymbol{\varepsilon}}), \\
\mathbf{M}^+ & \text{on } \partial Q^{\mathrm{ci}} \setminus \partial D^{\mathrm{ci}}, \\
\mathbf{M}^{\mathrm{G}}(\mathbf{M}, \mathbf{M}^+, \mathbf{a}_{\partial Q}) & \text{on } \partial Q^{\mathrm{nc}} \setminus \partial D^{\mathrm{nc}}, \\
\underline{\mathbf{M}} & \text{on } \partial Q \cap (\partial D^{\mathrm{ci}} \cup \partial D^{\mathbf{M}}),
\end{cases}
\tag{29}
$$

$$
\boldsymbol{\varepsilon}^* = \begin{cases}
\boldsymbol{\varepsilon} & \text{on } \partial Q^{\mathrm{co}} \cup (\partial Q \cap \partial D^{\mathbf{M}}), \\
\boldsymbol{\varepsilon}^+ & \text{on } \partial Q^{\mathrm{ci}} \setminus \partial D^{\mathrm{ci}}, \\
\boldsymbol{\varepsilon}^{\mathrm{G}}(\boldsymbol{\varepsilon}, \boldsymbol{\varepsilon}^+, \mathbf{a}_{\partial Q}) & \text{on } \partial Q^{\mathrm{nc}} \setminus \partial D^{\mathrm{nc}}, \\
\underline{\boldsymbol{\varepsilon}} & \text{on } \partial Q \cap (\partial D^{\mathrm{ci}} \cup \partial D^{\boldsymbol{\varepsilon}}),
\end{cases}
\tag{30}
$$

in which $\mathbf{M}$ and $\boldsymbol{\varepsilon}$ are interior traces, $\mathbf{M}^+$ and $\boldsymbol{\varepsilon}^+$ are exterior traces, $\mathbf{M}^{\mathrm{G}}$ and $\boldsymbol{\varepsilon}^{\mathrm{G}}$ are Godunov values, and $\underline{\mathbf{M}}$ and $\underline{\boldsymbol{\varepsilon}}$ are prescribed initial and boundary data. The Godunov values are functions of the interior and exterior traces and the volume vector $\mathbf{a}_{\partial Q}$ at each point on ∂Q^{nc}.[4]

3. Discontinuous Galerkin finite element method

3.1. Continuum strong form of the boundary value problem

We summarize the governing equation and jump conditions that comprise the strong form of our continuum boundary value problem.

Problem 2 (*Strong form*). Find $\mathbf{u} \in V$ such that for any regular $Q \subset D$,

$$
(\mathbf{dM} + \rho \mathbf{b})|_{Q \setminus \Gamma^J} = \mathbf{0},
\tag{31a}
$$

$$
(\mathbf{M}^* - \mathbf{M})|_{\partial Q \cup (Q \cap \Gamma^J)} = \mathbf{0},
\tag{31b}
$$

$$
(\boldsymbol{\varepsilon}^* - \boldsymbol{\varepsilon})|_{\partial Q} = \mathbf{0},
\tag{31c}
$$

$$
(\mathbf{u}_0^* - \mathbf{u}_0)|_{\partial Q^{\mathrm{ti}}} = \mathbf{0},
\tag{31d}
$$

---

[4] We omit a specification for $\mathbf{M}^*$ on $Q \cap \Gamma^J$; it is not required in our discontinuous Galerkin finite element formulation.

in which the values $\mathbf{M}^*$, $\boldsymbol{\varepsilon}^*$, $\mathbf{u}_0^*$ and $\mathbf{u}_0$ are defined as in Sections 2.3 and 2.6, $\boldsymbol{\varepsilon}$ is written in terms of $\mathbf{u}$ according to (3), and $\mathbf{M}$ is written as a function of $\boldsymbol{\varepsilon}$ according to the constitutive relation (23).

Remark 3. The jump condition (31d) is equivalent to $\int_{\partial Q^{\mathrm{ti}}} \mathbf{w} \wedge (\mathbf{u}^* - \mathbf{u}) \otimes \mathbf{i} \boldsymbol{\Omega} = 0$, $\quad \forall \mathbf{w} \in V_0^Q$. We use this alternative statement in the weak formulation below.

3.2. Causal partitions of the space–time domain D

Let $\mathscr{P} = \{Q_\alpha\}$ be a partition of D into open regions $Q_\alpha \subset D$, each with a regular boundary and such that $\partial Q_\alpha^{\mathrm{co}}$ has a nonzero measure. The subdomains Q_α are space–time finite elements in the discontinuous Galerkin formulation presented in the following sections. Let $\Gamma = \cup_{\alpha,\beta:\alpha\neq\beta} \overline{\partial Q_\alpha} \cap \overline{\partial Q_\beta}$. That is, Γ is a collection of d-manifolds on the boundary between adjacent subdomains in $\mathscr{P}$. $\mathscr{P}$ is a *causal partition* if all of the d-manifolds that comprise Γ are causal. $\mathscr{P}$ is a *patch-wise causal partition* if the subdomains Q_α can be grouped into patches of elements Q_β^* such that $\mathscr{P}^* = \{Q_\beta^*\}$ is a causal partition of D. From here on, we assume that all partitions $\mathscr{P}$ are at least patch-wise causal.[5] Note that the part of Γ associated with inter-element boundaries on the interior of a patch can be noncausal, but the part associated with inter-patch boundaries must be causal.

3.3. Weighted residual statement and weak formulation

The following discontinuous Galerkin finite element formulation weakly enforces the governing equations and jump conditions (31) on a finite set of subdomains in an energetically consistent manner. There are two sources of discretization error. First, we consider only a finite subset, rather than the complete set, of regular subdomains of D. Second, we use a finite-dimensional subspace of V^Q to approximate the solution on each subdomain Q.

Let $\mathscr{P}_h = \{Q_\alpha; \alpha = 1, \ldots, N\}$ be a partition of D into regular subdomains Q_α that is at least patch-wise causal. For each $Q \in \mathscr{P}_h$ we define a finite-dimensional solution space V_h^Q such that $V_0^Q \subset V_h^Q \subset H^2(Q, \mathbb{E}^d)$ and $\exists \mathbf{w} \in V_h^Q \ni \dot{\mathbf{w}} = \mathbf{v} \ \forall \mathbf{v} \in V_0^{Q}$.[6] The global solution space on D is the broken Sobolev space $V_h := \{\mathbf{w} \in BV(D, \mathbb{E}^d) : \mathbf{w}|_{Q \in \mathscr{P}_h} \in V_h^Q\}$, and we refer to the subdomains Q_α as *finite elements*. Given the structure of V_h^Q, we note that $Q \cap \Gamma^J = \emptyset$. Thus, the domains for (31b) and (31c) reduce to Q and ∂Q, respectively, in the discrete model.

From here on, a superposed '$\wedge$' indicates a function of the *weighting vector field* $\mathbf{w}$, and a subscript 'h' indicates a function of the discrete displacement solution $\mathbf{u}_h$. In particular, $\widehat{\mathbf{M}} = \mathbf{M}(\boldsymbol{\varepsilon}(\mathbf{w}))$, $\boldsymbol{\varepsilon}_h = \boldsymbol{\varepsilon}(\mathbf{u}_h)$, $\mathbf{M}_h = \mathbf{M}(\boldsymbol{\varepsilon}_h)$, and $\mathbf{u}_h^*$, $\mathbf{M}_h^*$ and $\boldsymbol{\varepsilon}_h^*$ follow from Eqs. (25), (29) and (30) with $\mathbf{u}$, $\mathbf{M}$, $\mathbf{M}^+$, $\boldsymbol{\varepsilon}$ and $\boldsymbol{\varepsilon}^+$ replaced by $\mathbf{u}_h$, $\mathbf{M}_h$, $\mathbf{M}_h^+$, $\boldsymbol{\varepsilon}_h$ and $\boldsymbol{\varepsilon}_h^+$. Also, $\mathbf{w}_0 := \sum_\alpha \langle \mathbf{w}_\alpha, \mathbf{w} \rangle_{\partial Q^{\mathrm{ti}}} \mathbf{w}_\alpha \in V_0^Q$.

Problem 4 (*Discrete weighted residual statement*). For each $Q \in \mathscr{P}_h$, find $\mathbf{u}_h \in V_h^Q$ such that

$$\int_Q \dot{\mathbf{w}} \wedge (\mathbf{dM}_h + \rho\mathbf{b}) + \int_{\partial Q} \{\dot{\mathbf{w}} \wedge (\mathbf{M}_h^* - \mathbf{M}_h) + (\boldsymbol{\varepsilon}_h^* - \boldsymbol{\varepsilon}_h) \wedge \mathbf{i}\widehat{\mathbf{M}}\} + \int_{\partial Q^{\mathrm{ti}}} \mathbf{w}_0 \wedge (\mathbf{u}_h^* - \mathbf{u}_h) \otimes \mathbf{i}\boldsymbol{\Omega} = 0, \ \ \forall \mathbf{w} \in V_h^Q. \quad (32)$$

Remark 5. The weighted residual statement (32) appears to be a Petrov–Galerkin method, because the residual of the governing Eq. (31a) is weighted by $\dot{\mathbf{w}}$ instead of $\mathbf{w}$. However, we can use the identity $\int_Q \dot{\mathbf{w}} \wedge (\mathbf{dM} + \rho\mathbf{b}) = -\int_Q \mathbf{w} \wedge \mathscr{L}(\mathbf{dM} + \rho\mathbf{b}) + \int_{\partial Q} \mathbf{w} \cdot \mathbf{i}(\mathbf{dM} + \rho\mathbf{b})$ to show that (32) is equivalent to a Bubnov–Galerkin method for the rate form of the equation of motion.

---

[5] Patch-wise causal partitions are important for the cases $d = 2, 3$ because it is difficult to generate strictly causal simplicial partitions for general space–time domain geometries in more than one spatial dimension.

[6] For polynomial bases, the latter requirement implies a minimum polynomial order $p_{\min} = 1$ for $d = 1$ and $p_{\min} = 2$ for $d = 2, 3$.

Remark 6. The third integral in (32) is dimensionally inconsistent. We could correct this by scaling the integrand by a factor $k^Q = \langle \|\mathbf{C}\| \rangle_Q / (h^Q)^2$, in which $\|\mathbf{C}\|$ is the operator norm of $\mathbf{C}$, $\langle \cdot \rangle_Q$ indicates an average over element Q, and h^Q is the spatial diameter of element Q.[7] In practice, it is important to maintain dimensional consistency to avoid possible conditioning problems. We nonetheless omit k^Q in (32) and in related integrals below for simplicity.

Applying the Stokes theorem and noting that

$$\mathbf{w}_0 \wedge (\mathbf{u}_h^* - \mathbf{u}_h) \otimes \mathbf{i\Omega} = \{\mathbf{w}_0 \cdot (\mathbf{u}_h^* - \mathbf{u}_h)\}\mathbf{i\Omega},$$

we obtain the weak form of Problem 4.

Problem 7 (*Discrete weak form*). For each $Q \in \mathscr{P}_h$, find $\mathbf{u}_h \in V_h^Q$ such that

$$\int_Q \{-\mathbf{d}\dot{\mathbf{w}} \wedge \mathbf{M}_h + \dot{\mathbf{w}} \wedge \rho \mathbf{b}\} + \int_{\partial Q} \{\dot{\mathbf{w}} \cdot \mathbf{M}_h^* + (\boldsymbol{\varepsilon}_h^* - \boldsymbol{\varepsilon}_h) \wedge \mathbf{i\widehat{M}}\} + \int_{\partial Q^{\mathrm{ti}}} \{\mathbf{w}_0 \cdot (\mathbf{u}_h^* - \mathbf{u}_h)\}\mathbf{i\Omega} = 0, \quad \forall \mathbf{w} \in V_h^Q. \tag{33}$$

This is the formulation used in our numerical implementation.

Remark 8. Since $V_0^Q \subset V_h^Q$, and because the first two integrals in (32) vanish identically for all $\mathbf{w} \in V_0^Q$, the discrete solution $\mathbf{u}_h$ satisfies

$$\int_{\partial Q^{\mathrm{ti}}} \mathbf{w}_0 \wedge (\mathbf{u}_h^* - \mathbf{u}_h) \otimes \mathbf{i\Omega} = 0, \quad \forall \mathbf{w} \in V_h^Q.$$

In view of the inclusion of the finite-dimensional space V_0^Q within the discrete space V_h^Q, this implies that (10b) is enforced strongly.

Remark 9. Consideration of all weighting functions of the form $\mathbf{w} = t(\mathbf{c} + \mathbf{S}x) \in V_h^Q$ in (33) (cf. (4)), leads to the conclusion that the discrete solution $\mathbf{u}_h$ satisfies exactly the integral forms of balance of linear momentum (12) and balance of angular momentum (14) on every $Q \in \mathscr{P}_h$.

4. Summary analysis of the method

4.1. Additional notation

This section reviews analysis results from [21] concerning stability and error estimates for the proposed method. Here we introduce some additional notation needed for the review.

For any $Q \subset D$, let

$$a_Q(\mathbf{u}, \mathbf{w}) := -\int_Q \dot{\mathbf{w}} \wedge (\mathbf{dM}) - \int_{\partial Q} \{\dot{\mathbf{w}} \wedge (\mathbf{M}^* - \mathbf{M}) + (\boldsymbol{\varepsilon}^* - \boldsymbol{\varepsilon}) \wedge \mathbf{i\widehat{M}}\} - \int_{\partial Q^{\mathrm{ti}}} \mathbf{w}_0 \wedge (\mathbf{u}^* - \mathbf{u}) \otimes \mathbf{i\Omega}, \tag{34}$$

$$(\dot{\mathbf{w}}, \rho\mathbf{b})_Q := \int_Q \dot{\mathbf{w}} \wedge \rho\mathbf{b}. \tag{35}$$

---

[7] For example, for $d = 1$ with uniform material properties in element Q, we define $\|\mathbf{C}\| := \max_{\boldsymbol{\varepsilon}} \frac{\|\mathbf{C}\boldsymbol{\varepsilon}\|_{\sigma+\mathbf{p}}}{\|\boldsymbol{\varepsilon}\|_{\varepsilon}}$, $\|\boldsymbol{\varepsilon}\|_{\varepsilon} := \sqrt{(E_{11})^2 + \frac{1}{c^2}(\dot{u}_1)^2}$ and $\|\boldsymbol{\sigma} + \mathbf{p}\|_{\sigma+\mathbf{p}} := \sqrt{(\sigma^{11})^2 + c^2(p^1)^2}$ in which c is the fastest wave speed. Then we get $c^2 = E/\rho$, so that $\|\mathbf{C}\| = E$, where E is Young's modulus, and $k^Q = E/(h^Q)^2$.

Note that $a_Q(\mathbf{u}, \mathbf{w})$ is linear in $\mathbf{w}$ and affine in $\mathbf{u}$. The weighted residual statement (32) is rewritten as

$$a_Q(\mathbf{u}, \mathbf{w}) = (\dot{\mathbf{w}}, \rho\mathbf{b})_Q. \tag{36}$$

We restrict our attention to partitions $\mathscr{P}$ of D that are at least patch-wise causal and that are comprised of simplex elements in $\mathbb{E}^d \times \mathbb{R}$ with $d + 2$ vertices per element. We make the usual assumptions that the mesh is nondegenerate (i.e., the ratio of the diameters of the smallest sphere containing Q and the largest sphere contained in Q is uniformly bounded), and quasi-uniform (i.e., there exists a characteristic diameter h for which the ratio of h and the diameter of the smallest sphere containing Q, and the reciprocal of this ratio, are bounded).

The patch-wise causal property of $\mathscr{P}_h$ ensures that there exists a partial ordering of patches such that the solution in any given patch is independent of the solutions on all patches that appear later in the ordering. The solution advances one patch at a time within a direct patch-by-patch solution procedure for Problem 7. It is convenient to group the patches in $\mathscr{P}_h$ into layers that represent D in a front-like fashion. The initial front $\mathscr{F}_0$ is the inflow boundary $\mathscr{F}_0 = \partial D^{\mathrm{ti}}$. We use the partial ordering to define layers of patches and their associated fronts. For $k \geqslant 1$, the kth layer S_k contains all elements whose causal inflow boundaries belong to the $(k-1)$th front:

$$S_k := \{Q : \partial Q^{\mathrm{ci}} \subset \mathscr{F}_{k-1}\}. \tag{37}$$

The kth front is the outflow boundary of layer S_k and is related to the previous front according to

$$\mathscr{F}_k = (\mathscr{F}_{k-1} \setminus \partial S_k^{\mathrm{ci}}) \cup \partial S_k^{\mathrm{co}}, \quad k = 1, 2, \ldots \tag{38}$$

Fig. 3 shows the configuration of the layers as well as the fronts, $\mathscr{F}_1$ and $\mathscr{F}_2$, for a partial partition of D corresponding to an intermediate stage of the solution process.

For any Q in $\mathscr{P}_h$, let $\mathbf{f}$ be any field on Q with the trace property on ∂Q. We use $[\![\mathbf{f}]\!] := \mathbf{f}^* - \mathbf{f}$ to denote the difference between the target value for $\mathbf{f}$ and the trace of $\mathbf{f}$ on ∂Q.

4.2. Inner products and norms

Let $\|\mathbf{u}\|_Q$ and $\|\mathbf{u}\|_{n,Q}$ denote the $L^2(Q, \mathbb{E}^d)$ and $H^n(Q, \mathbb{E}^d)$ norms, respectively. We define an inner product $\langle \cdot, \cdot \rangle_{e,Q}$ on V^Q by

$$\langle \mathbf{u}, \mathbf{w} \rangle_{e,Q} := \int_Q \{(\mathbf{u} \cdot \mathbf{w})\mathbf{\Omega} + \boldsymbol{\varepsilon}(\mathbf{u}) \wedge \mathbf{C}\boldsymbol{\varepsilon}(\mathbf{w})\} \tag{39}$$
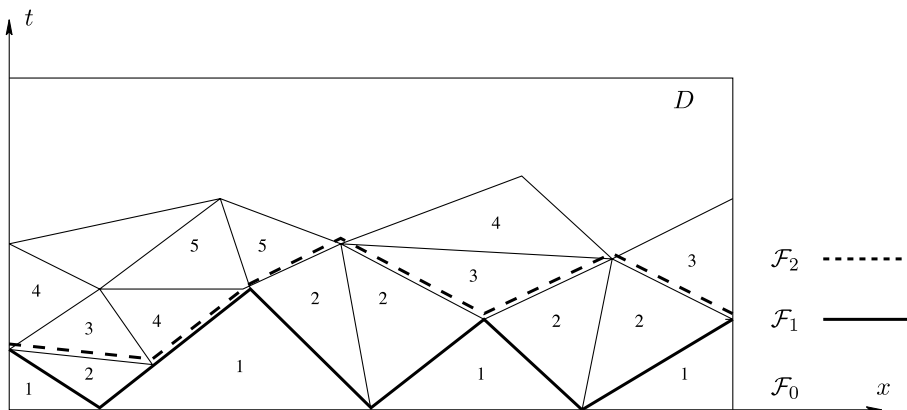

Fig. 3. Partial ordering of patches, layer definitions and front ordering.

and we denote its induced norm by $\|\mathbf{u}\|_{e,Q}$. We also define $|\mathbf{u}|_{e,Q}$, a semi-norm on V^Q that is a full norm on V_ε^Q:

$$|\mathbf{u}|_{e,Q}^2 := \int_Q \boldsymbol{\varepsilon} \wedge \mathbf{C}\boldsymbol{\varepsilon} = 2 \int_Q \boldsymbol{\Phi}. \tag{40}$$

Let $\Gamma \subset D$ be an inclined d-manifold, and let $\mathbf{v}$ be a vector field on D with the trace property on Γ. We define the seminorm $|\cdot|_\Gamma$ by

$$|\mathbf{v}|_\Gamma^2 := -\int_\Gamma |\mathbf{v}|^2 \mathbf{i}\boldsymbol{\Omega}. \tag{41}$$

For any $Q \in \mathscr{P}_h$, $|\cdot|_{\partial Q^{\mathrm{ti}}}$ is a full norm on V_0^Q. We also define a seminorm on $V(D)$ [21],

$$|\mathbf{u}|_{e,\Gamma}^2 := -\int_\Gamma \mathbf{i}(\boldsymbol{\varepsilon} \wedge \mathbf{C}\boldsymbol{\varepsilon}) = -2 \int_\Gamma \mathbf{i}\boldsymbol{\Phi}. \tag{42}$$

4.3. Dissipation and stability

Setting $\mathbf{w} = \mathbf{u} = \mathbf{u}_h$ in (33) and recalling Remark 8, we obtain an expression for Δ_Q the numerical energy dissipation over $Q \in \mathscr{P}_h$ with respect to the target energy flux on ∂Q:

$$\Delta_Q := \int_Q \dot{\mathbf{u}}_h \cdot \rho \mathbf{b} + \frac{1}{2} \int_{\partial Q} \{\dot{\mathbf{u}}_h^* \cdot \mathbf{M}_h^* + \boldsymbol{\varepsilon}_h^* \wedge \mathbf{i}\mathbf{M}_h^*\} = \frac{1}{2} \int_{\partial Q} \{[\![\dot{\mathbf{u}}_h]\!] \cdot [\![\mathbf{M}_h]\!] + [\![\boldsymbol{\varepsilon}_h]\!] \wedge [\![\mathbf{i}\mathbf{M}_h]\!]\}. \tag{43}$$

We have exact energy balance on Q when the jump integral on the right-hand side of (43) vanishes. The total energy dissipation over D with respect to the target flux on ∂D, denoted by Δ, is given by

$$\Delta := \int_D \dot{\mathbf{u}}_h \cdot \rho \mathbf{b} + \frac{1}{2} \int_{\partial D} \{\dot{\mathbf{u}}_h^* \cdot \mathbf{M}_h^* + \boldsymbol{\varepsilon}_h^* \wedge \mathbf{i}\mathbf{M}_h^*\} = \sum_{Q \in \mathscr{P}_h} \Delta_Q. \tag{44}$$

Both Δ and Δ_Q can be shown to be non-negative in the case of patch-wise causal partitions [21]. Thus, our method is dissipative.

The following stability estimate is proven in [21] for $d = 1, 2$, for homogeneous data on ∂D^{nc} and for patch-wise causal partitions where all of the interior noncausal faces are vertical and the polynomial degree n in each element $Q \in \mathscr{P}_h$ does not exceed the number of noncausal faces in Q.[8]

$$\max_{1 \leqslant k \leqslant M} \sum_{F \in \mathscr{F}_k} (|\mathbf{u}_h^*|_F^2 + |\mathbf{u}_h^*|_{e,F}^2) + \sum_{Q \in \mathscr{P}_h} \{\|\mathbf{u}_h\|_{e,Q}^2 + |[\![\mathbf{u}_h]\!]|_{e,\partial Q}^2\}$$
$$\leqslant C \left\{ |\underline{\mathbf{u}}|_{\partial D^{\mathrm{ti}}}^2 + \int_{\partial D^{\mathrm{ci}}} \{\underline{\dot{\mathbf{u}}} \wedge \underline{\mathbf{M}} + \underline{\boldsymbol{\varepsilon}} \wedge \underline{\mathbf{i}\mathbf{M}}\} + \|\rho \mathbf{b}\|_D^2 \right\}. \tag{45}$$

4.4. Error estimate

Let $\mathbf{u}_h$ be a solution to Problem 7 and let $\mathbf{u}$ be the solution of the continuum version of Problem 7. In the continuum version, we consider all $Q \subset D$, seek $\mathbf{u} \in V^Q$ rather than $\mathbf{u}_h \in V_h^Q$, and consider all weightings $\mathbf{w} \in V^Q$. The following theorem bounds the error $\mathbf{u}_h - \mathbf{u}$ in a suitable mesh-dependent norm.[9]

---

[8] Extensions for inclined interior noncausal faces, for $d = 3$ and for higher values of n appear to hold, but are not proven in [21].
[9] The proof of this theorem is done for $d = 1, 2$ in [21] and may be extended for $d = 3$. Our numerical experience indicates that the estimate holds for any polynomial degree n.

Let $\mathscr{P}_h$ be a patch-wise causal partition of the space–time domain $D \subset \mathbb{E}^d \times \mathbb{R}$ in which all of the non-causal boundaries are vertical, and let $\mathbf{u} \in H^n(D, \mathbb{E}^d)$. Assume that for every simplex element $Q \in \mathscr{P}_h$, the polynomial degree n does not exceed the number of causal faces in Q. Then $\mathbf{u}_h - \mathbf{u}$ satisfies the bound

$$\Psi := \Psi_{\mathscr{F}} + \Psi_D \leqslant Ch^{2n-1}\|\mathbf{u}\|^2_{n+1,D}, \tag{46}$$

in which

$$\Psi_{\mathscr{F}} := \max_{1 \leqslant k \leqslant M} \sum_{F \in \mathscr{F}_k} (|\mathbf{u}_h^* - \mathbf{u}^*|_F^2 + |\mathbf{u}_h^* - \mathbf{u}^*|_{e,F}^2), \tag{47}$$

$$\Psi_D := \sum_{Q \in \mathscr{P}(D)} (\|\mathbf{u}_h - \mathbf{u}\|_{e,Q}^2 + \|[\![\mathbf{u}_h - \mathbf{u}]\!]\|_{e,\partial Q^{ci}}^2). \tag{48}$$

5. Implementation

This section describes our implementation of the space–time discontinuous Galerkin procedure. In particular, we discuss the construction of patch-wise causal unstructured space–time meshes and an associated advancing-front solution technique that offers linear complexity in the number of space–time elements (assuming uniform polynomial order over the elements). We also briefly describe special post-processing techniques for visualizing solution data that are computed and stored on unstructured space–time meshes.

5.1. Meshing the space–time domain

We use the Tent Pitcher algorithm [22,23] to construct unstructured, patch-wise causal space–time meshes. Tent Pitcher is extensible to the case $d = 3$, but has so far been implemented only for $d = 1, 2$. Here we focus on the case $d = 2$. Given a triangulated spatial domain ω and a terminal time T, Tent Pitcher constructs a tetrahedral mesh over the space–time domain $\omega \times [0, T]$. The algorithm is designed for implementation as an advancing front procedure, which alternately constructs a new causal patch of elements and computes a solution of Problem 7 within the new patch.

At every iteration of the meshing procedure, the *front* is the graph of a continuous function $t : \omega \to \mathbb{R}$, such that t is linear within every element in the triangulation of ω. In other words, the front is a terrain comprised of inclined triangular facets that correspond to the triangles in the underlying space mesh over ω. Tent Pitcher advances the front by selecting an arbitrary local minimum vertex on the front and advancing that vertex in time to define a new configuration of the front.[10] The vertical segment between the old and new positions of the vertex is called a *tent pole*, and the volume between the old and new configurations of the front is called a *tent*. Tent Pitcher decomposes each new tent into a patch of simplex finite elements (tetrahedra for $d = 2$) that share the tent pole as a common vertical edge. The height of the tent pole is limited by the requirement that each new facet in the front must satisfy the causality constraint (28). In addition, a *progress constraint* might limit the tent pole height; this guarantees that the Tent Pitcher algorithm can progress to a new configuration in all future iterations. Fig. 4 shows a sequence of Tent Pitcher iterations, starting from the spatial triangulation as the initial configuration of the front.

5.2. Advancing-front solution procedure

Every time Tent Pitcher advances the front, it passes the new patch of finite elements to the routines that solve the space–time discontinuous Galerkin Problem 7. In addition to the new patch, Tent Pitcher also

---

[10] In practice, various heuristics can be used to select a specific vertex when more than one local minimum is available. In parallel computing environments, more than one vertex can be advanced simultaneously.
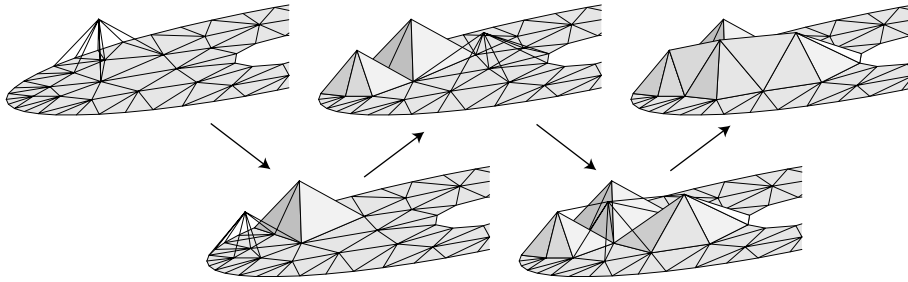
Fig. 4. Pitching tents in space–time.

passes the previously solved elements that are adjacent to the new patch across the old configuration of the front. The solutions on these elements provide the inflow data for the new patch. Various flags and physical data are also passed, so the finite element routines have all of the necessary information to assemble and solve the finite element equations on the patch. The elements that surround a given tent pole share vertical noncausal faces. Thus, the elements within a single patch must be solved simultaneously.

Elements are retained in high-speed storage as long as they remain adjacent to the front. Once they are no longer adjacent to the current front configuration, they are no longer needed and can be written out to a mass storage device. If all of the space–time finite elements use the same set of basis functions (for example, if they have the same polynomial order) and if the degree of every vertex in the spatial triangulation in bounded, then the storage requirements and computational complexity per patch are each bounded, and the overall complexity scales linearly with the number of elements in the space–time mesh.

5.3. Visualization

Visualization of data computed on unstructured space–time grids poses special challenges. The data might be discontinuous and are often represented with high-order basis functions. The data are not referenced by uniform time steps, constant-time slices through the data generally do not coincide with element boundaries, and the grid might be nonconforming. Linear interpolations used by many graphics rendering systems cannot represent accurately our high-order solutions. These attributes make standard visualization technology unsuitable for our purposes.

We use a special per-pixel accurate visualization system [28] that is responsive to the above requirements and that exploits the high-performance features and programmability of contemporary GPUs. For any constant-time slice, our system computes two scalar fields that are mapped into a height field and a color field for display. The first step is to identify all of the space–time elements that are intersected by a given constant-time plane and to compute the intersection of each tetrahedral element with the plane. This generates a set of polygons (triangles and quadrilaterals) that is used to render a single frame of animation or a still image.

The next step is to render the scalar fields on the time-slice polygon mesh. For each polygon, we download to the GPU descriptions of the solution coefficients and the finite element basis functions that model the space–time displacement field within the polygon's parent tetrahedron. We also download to the GPU software for evaluating one or more scalar solution fields, such as the strain energy density. The GPU uses the finite element basis functions to evaluate the scalar field at every rendered pixel location; this provides a precise map of the discrete solution into color on the display screen. The pixel-level computations are accelerated by the deeply pipelined and parallel architecture of the GPU. It turns out that it is not practical to use this approach for the scalar quantity that is mapped to the height field. Instead, we use adaptive subdivision of the time-slice polygons to attain the desired accuracy. See [28] for a more detailed description of the visualization system and of the importance of per-pixel accurate rendering.

6. Numerical examples

This section presents numerical examples that verify the predicted performance of the new finite element formulation and demonstrate its modeling capabilities. First, we investigate the convergence rates of various error measures for two problems, one where the exact solution is smooth and one with weak shocks where the regularity of the exact solution limits the convergence rates according to the error estimate (46).[11] We also examine the impact of using true Godunov values as the target values on noncausal interfaces in comparison to using simple average values. The section closes with a simulation of shock propagation in a solid-fuel rocket grain that demonstrates the ability of the method to capture complex shock patterns with exact momentum balance and very low energy dissipation.

6.1. Convergence studies

This subsection presents convergence studies for plane stress models based on the error measures given in (44), (46) and (47) as well as a front-based displacement error measure $\Psi_{\mathbf{u}}$:

$$\Psi_{\mathbf{u}} := \max_{1 \leqslant k \leqslant M} \sum_{F \in \mathscr{F}_k} |\mathbf{u}_h^* - \mathbf{u}^*|_F^2. \tag{49}$$

All of the error measures are normalized by the *total inflow energy* $\mathbf{E}_0$ in the results reported below. We assume an isotropic linearly elastic material with Young's modulus $E = 1$, Poisson ratio $v = 0.3$, and $\rho = 1$.

The use of Godunov values for the target values of $\mathbf{M}$ and $\boldsymbol{\varepsilon}$ on interior noncausal interfaces distinguishes the present formulation from some others in which averaged values are used. To evaluate the impact of this difference, we also present results for a modified method in which the target values on $\partial Q^{nc} \backslash \partial D^{nc}$ are redefined as

$$\mathbf{M}^* = \mathbf{M}^A := \frac{1}{2}(\mathbf{M}^+ + \mathbf{M}), \tag{50a}$$

$$\boldsymbol{\varepsilon}^* = \boldsymbol{\varepsilon}^A := \frac{1}{2}(\boldsymbol{\varepsilon}^+ + \boldsymbol{\varepsilon}). \tag{50b}$$

6.1.1. Approximation of a smooth solution
The displacement field whose components are given by

$$u_1 = m_1 A \sin(m_1 x^1) \sin(m_2 x^2) \sin\left(\sqrt{m_1^2 + m_2^2}\hat{c}_p t\right),$$

$$u_2 = -m_2 A \cos(m_1 x^1) \cos(m_2 x^2) \sin\left(\sqrt{m_1^2 + m_2^2}\hat{c}_p t\right), \tag{51}$$

where $m_1, m_2 \in \mathbb{R}$ and $\hat{c}_p$ is defined in Eq. (B.2), satisfies the equation of motion in $\mathbb{E}^2 \times \mathbb{R}$. We apply initial conditions and boundary conditions that are consistent with this field over the spatial domain $\omega = [0, 2] \times [0, 1]$ and compute the approximation of (51) via the discontinuous Galerkin method, Problem 7. We select $A = \pi^{-1}$, $m_1 = \pi$ and $m_2 = 2\pi$ to generate a single complete wave over ω in both spatial directions. The terminal time of the simulation is $2\pi\hat{c}_p/\sqrt{m_1^2 + m_2^2} = 0.85323$, which represents one complete cycle. The spatial discretization is based on square regions with edge-length h; each square is subdivided

---

[11] By *weak shock* we mean a solution feature where the displacement field remains continuous, but the displacement derivatives exhibit jumps.

into two triangles. The finite element basis in each space–time tetrahedron generated by Tent Pitcher consists of a complete polynomial of degree $p = 2, 3, 4, 5$.

The convergence rates for the total error measure Ψ reported in Fig. 6(a) confirm the predicted rate of $2p - 1$ when the Godunov values are used (cf. (46)). The same convergence rates are attained when averaged values are used, but the magnitude of the error is slightly larger in each case. Similar results appear in Fig. 6(b) for the numerical energy dissipation Δ, where both Godunov and averaged values deliver a convergence rate of $2p - 1$ and nearly identical error magnitudes.

Optimal convergence rates of $2p + 2$ and $2p$ are achieved for the front-based error measures, $\Psi_{\mathbf{u}}$ and $\Psi_{\mathscr{F}}$, as shown in Fig. 7(a) and (b). Little difference is seen between the magnitudes of $\Psi_{\mathbf{u}}$ obtained with Godunov and averaged values; however, the Godunov values deliver slightly smaller values for $\Psi_{\mathscr{F}}$.

A careful examination of Eqs. (B.1) and (B.3) reveals that the Godunov values equal the averaged values plus a jump term. Since the jump terms tend to zero as the approximate solutions converge to the smooth exact solution, we expect little difference between the two approximations. Thus, we conclude that the averaged values might be preferred, due to their simple form, for problems with smooth solutions. However, bigger differences are expected when the exact solution is not smooth and the jump terms do not vanish in the limit of mesh refinement. This case is studied in the next example.
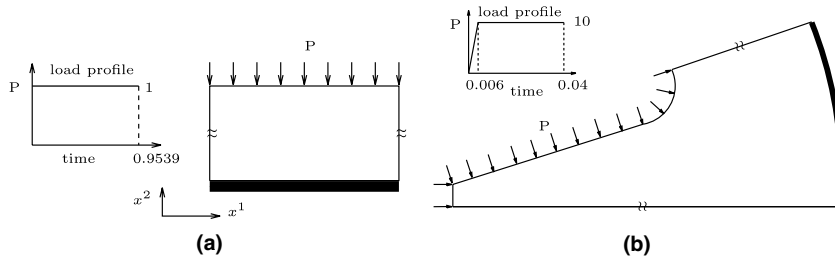
Fig. 5. Spatial domains and boundary conditions for the numerical examples: (a) step-function pressure load on an infinite strip, (b) shock pressure load on a segment of a solid-fuel rocket grain.
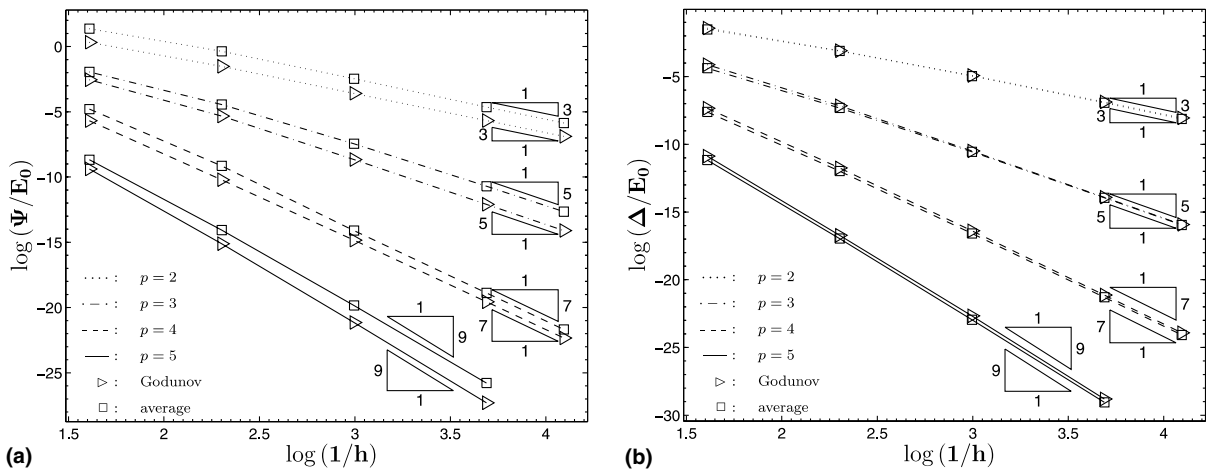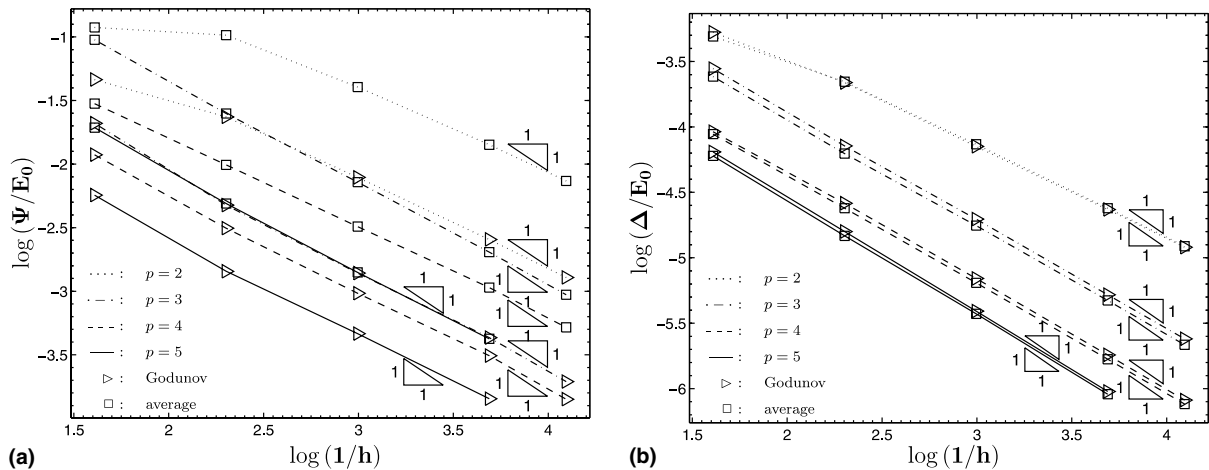

Fig. 6. Convergence rates for the approximation of a smooth solution: (a) convergence of the total error measure Ψ, (b) convergence of the numerical energy dissipation Δ.

6.1.2. Approximation of a solution with a weak shock

We consider an infinite strip with unit width, as shown in Fig. 5(a). A uniform pressure P is applied to the top edge of the strip, and the bottom edge is fixed. The history of the load intensity P is a step-function centered at time zero. This creates a dilatational shock wave, which traverses the strip until it reaches the bottom edge at the end of the simulation time interval. We use symmetry boundary conditions to restrict our model to a strip of length 2 in the x^2 direction.

Fig. 8(a) shows the convergence rates for the total error measure Ψ. In this case, the approximation based on Godunov values clearly outperforms the approximation that uses averaged values. Note that the convergence rate is unity in all cases, because the exact solution $\mathbf{u}$ does not satisfy the regularity requirement for (46). Fig. 8(b) compares the numerical energy dissipation Δ for the alternative target value
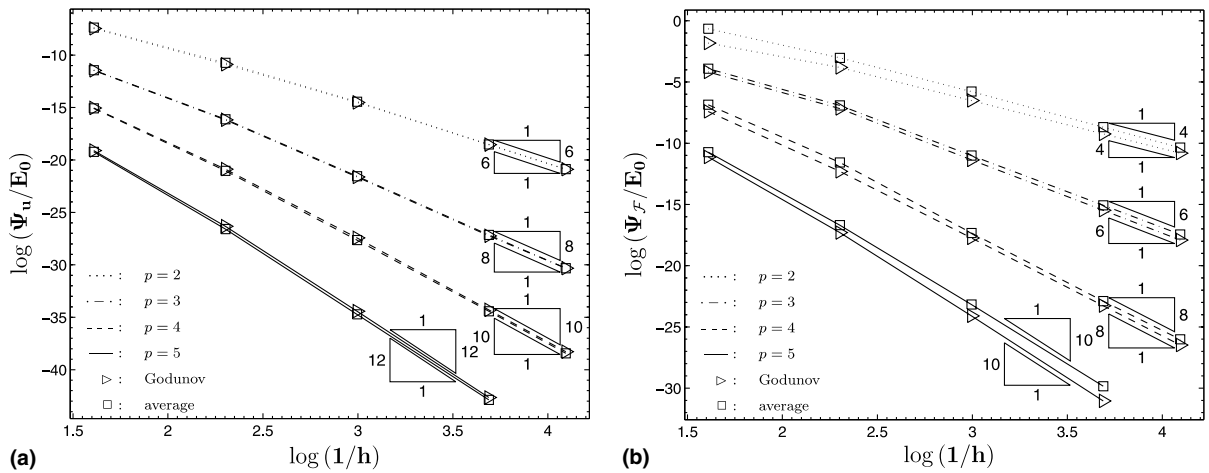
Fig. 7. Convergence rates for the front-based error measures; smooth solution: (a) convergence of the front-based displacement error $\Psi_{\mathbf{u}}$, (b) convergence of the front-based error measure $\Psi_{\mathscr{F}}$.

Fig. 8. Convergence rates for the approximation of a solution with a weak shock: (a) convergence of the total error measure Ψ, (b) convergence of the numerical energy dissipation Δ.

definitions. Similar to the results for the smooth solution case, the results for this error measure are nearly the same for the averaged and Godunov target values.

One possible explanation for the qualitative difference between the results for Ψ and Δ is the fact that Δ only measures errors on the element outflow boundaries, a region where discontinuous Galerkin methods typically deliver their most accurate results. On the other hand, Ψ measures errors on the element interiors as well as on the complete element boundaries, so it is a more stringent error indicator than Δ. These results suggest that the use of Godunov target values can be beneficial in problems involving shocks. However, averaged target values can still be used to good effect when algorithmic simplicity is a priority.
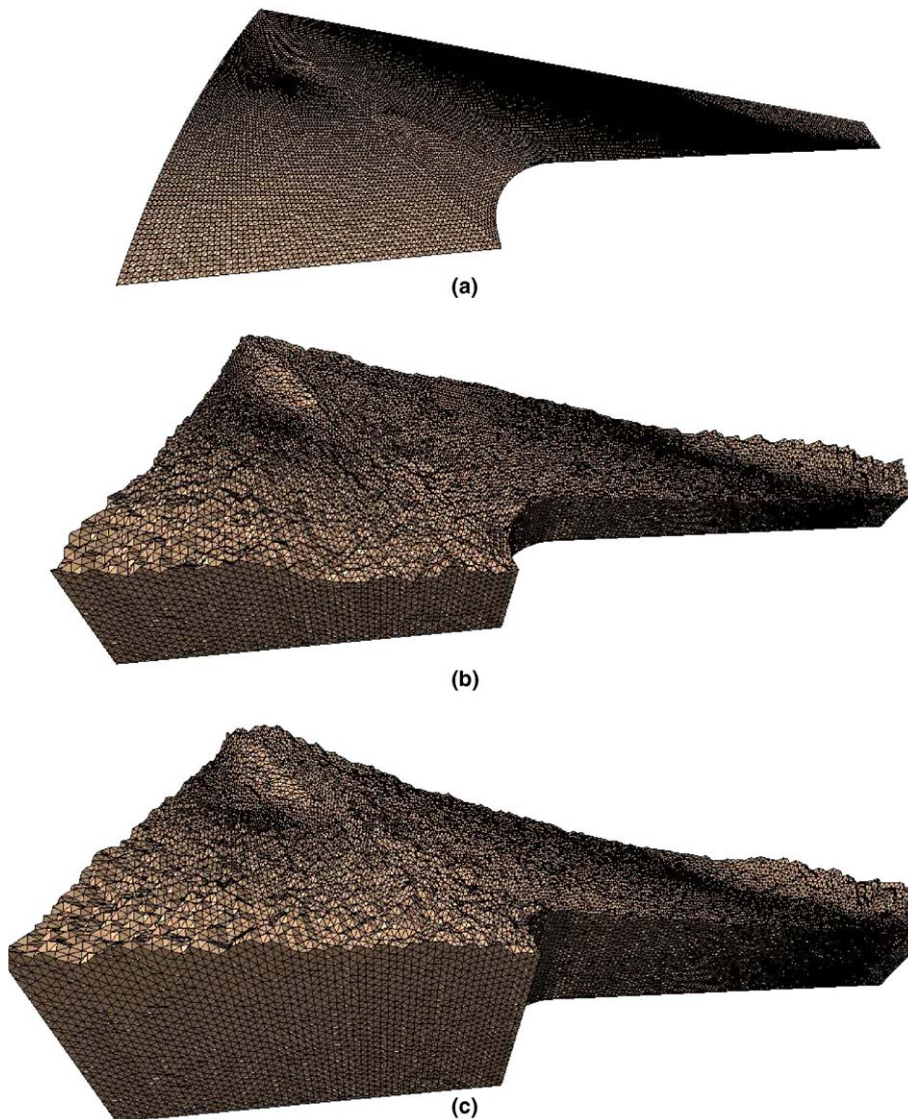
Fig. 9. Evolution of the space–time mesh for the solid-fuel rocket grain example: (a) initial space mesh, (b) partial space–time mesh containing 1.4 million tetrahedra, (c) partial space–time mesh containing 2.8 million tetrahedra.
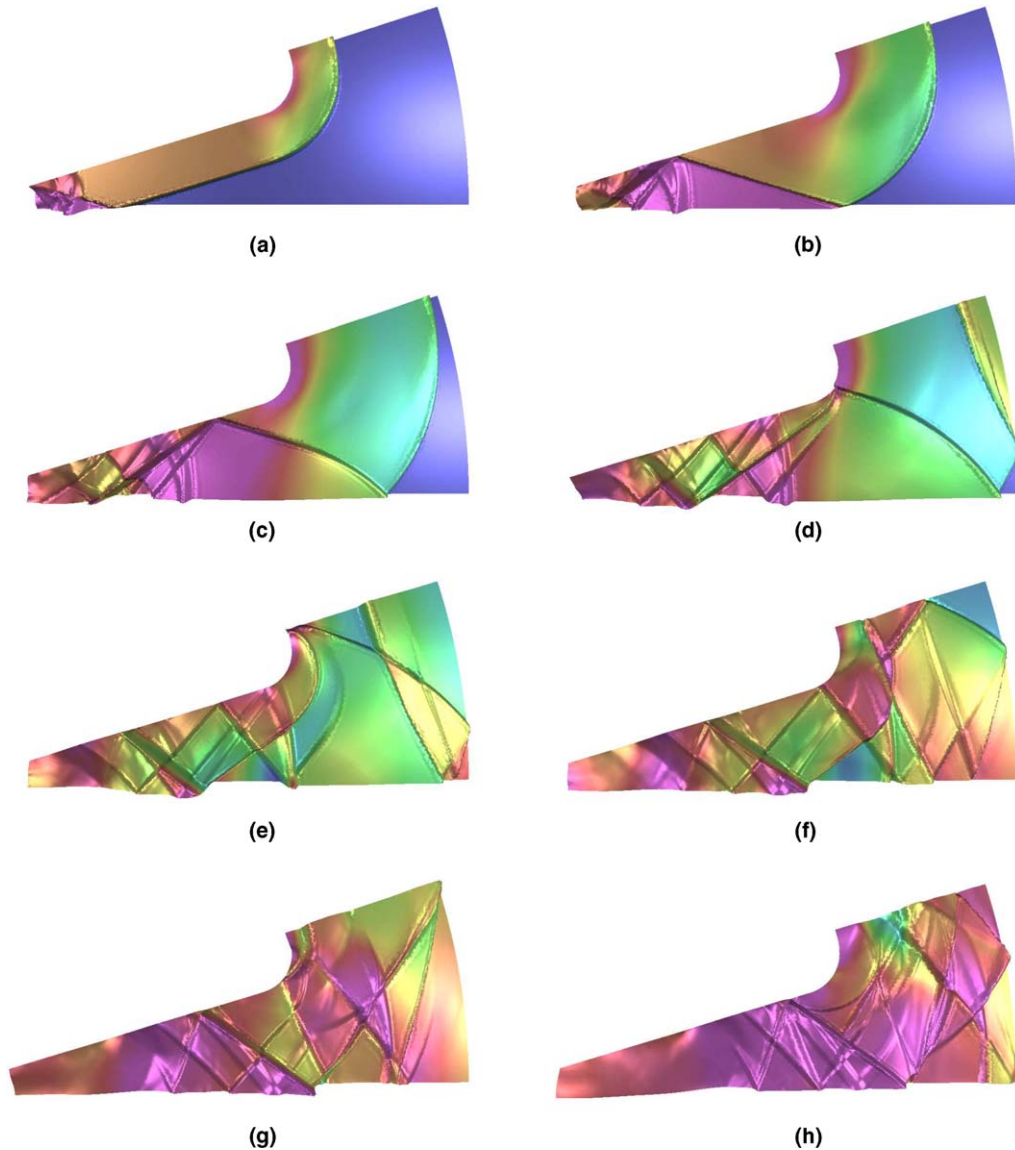
Fig. 10. Elastic shock propagation in a segment of a solid-fuel rocket grain: (a) time $t = 0.050$, (b) time $t = 0.100$, (c) time $t = 0.150$, (d) time $t = 0.200$, (e) time $t = 0.250$, (f) time $t = 0.300$, (g) time $t = 0.350$, (h) time $t = 0.400$.

6.2. Solid-fuel rocket grain subjected to a sudden pressure load

Fig. 5(b) shows a single sector of a 2D cross-section of a star shaped solid-fuel rocket grain. We use a plane strain model, with Young's modulus $E = 10$, Poisson ratio $v = 0.25$, and density $\rho = 2$. Symmetry boundary conditions are applied along the straight edges at the top and bottom, and the outer skin is modeled by a fixed boundary condition. A pressure P is applied uniformly over the interior surfaces as shown; the magnitude of P ramps rapidly from zero to a maximum value of 10 at time $t = 0.006$ and holds constant at that value until the simulation interval terminates at time $t = 0.400$. This load history approximates (very

roughly) the sudden pressurization of the grain as combustion initiates within the rocket core. Our goal is to study the resulting pattern of shock waves in the grain.

Fig. 9 shows the initial space mesh and two partial space–time meshes constructed by Tent Pitcher during the course of the simulation. We use complete cubic polynomials to model the displacement field within each space–time tetrahedron. The complete space–time mesh contains a total of 22 million tetrahedra arranged in 3.8 million patches. This discretization yielded a total numerical energy dissipation of only 0.025% of the inflow energy due to the pressure loading. Linear and angular momentum balance to within machine precision.

Fig. 10 shows a time sequence of visualizations of the solution generated by the per-pixel visualization system [28] described in Section 5.3. The strain energy density field is mapped to color, with blue indicating zero energy density. The velocity magnitude is mapped to the height field, which is then shaded by a lighting model to reveal its form. This visualization clearly reveals the propagation of the initial shock and its numerous reflections. The shock fronts are well resolved. Some overshoot and undershoot is evident ahead of and behind each shock front, as we have not added any stabilization to the basic Galerkin formulation. However, these artifacts are benign in that they leave no trace once a shock front passes a given location.

7. Conclusions

We have presented a new space–time formulation of linearized elastodynamics that supports a discontinuous (Bubnov-)Galerkin finite element method that balances exactly both linear and angular momentum on every space–time element. Balance is defined with respect to Godunov boundary values—the physically meaningful and mathematically correct values when shocks are present. Our numerical experiments confirm that the use of Godunov values on interior noncausal interfaces generates smaller errors than alternative averaging schemes in problems with shocks.

Our method is dissipative and unconditionally stable. We have focused in this paper on partitions of the space–time domain that are at least patch-wise causal, a property that enables solution strategies with linear complexity in the number of space–time elements when the polynomial order is fixed. However, the discrete weak form Problem 7 remains valid on arbitrary partitions. Indeed, numerical experiments (not reported in this work) confirm that partitions with arbitrarily long time steps can be used, albeit at the expense of foregoing the patch-by-patch solution procedure and the linear complexity property.

Although our method does not balance energy exactly, the numerical dissipation is relatively small. There is no need for filtering or extra stabilization. Our numerical studies confirm the error estimate (46) and suggest that the limits on the polynomial degree used to facilitate the proof of the estimate in [21] are not essential. We also found that our method delivers optimal convergence rates with respect to the front-based error measures, $\Psi_{\mathbf{u}}$ and $\Psi_{\mathscr{F}}$.

Several enhancements and extensions of our formulation and implementation are worthy of mention. We have tested a parallel version of the interleaved mesh-generation and solution algorithm described in Section 5. The algorithms are relatively easy to parallelize, and we achieved linear scaling with better than 95% processor utilization on clusters of up to 64 processors. An adaptive extension of Tent Pitcher [23] has been shown to greatly increase efficiency by introducing mesh refinement only along the space–time trajectories of propagating shocks and singular solution features (e.g., crack tips). The support for nonconforming space–time grids in our SDG method facilitates strongly graded adaptive meshes. Integration and assembly of patch-level systems accounts for a relatively large percentage of our computational load; equation solving is limited to systems of relatively modest size. In fact, a large share of the integration calculations are redundant, and a substantial reduction in computational cost could be realized through the use of *quadrature free methods*, as in [29].

Applications-based research motivates several other improvements. For example, we have implemented a cohesive damage model that simulates fracture and other debonding phenomena. Implementation of cohesive traction–separation laws within our discontinuous Galerkin framework is straightforward: relaxation of the kinematic compatibility constraint (10) and the substitution of the cohesive constitutive relation for the target tractions along the cohesive interface. We are investigating further extensions of the Tent Pitcher algorithm that would support inclined tent poles and more general transformations of the advancing front. We plan to use these generalizations in boundary-tracking algorithms for applications with moving interfaces and moving boundaries. We are also considering generalizations of the formulation to accommodate finite deformations and nonlinear material models.

Acknowledgements

Appendix A. Component expressions for the weak formulation

This appendix presents an alternative statement of the weak form (33) using conventional tensor component expressions. First, however, we must introduce a mapping of the space–time from $\mathbb{E} \times \mathbb{R}^d$ to $\mathbb{E}^{d+1}$ to enable the construction of normal vector fields on space–time d-manifolds. This mapping establishes an arbitrary metric on space–time that is not intrinsic to elastodynamics. While it compromises the formal invariance of our formulation, it introduces no error. Specifically, we introduce an arbitrary reference velocity magnitude c and define a *pseudo-time*, $\tilde{t} = ct$, whose dimension is length. All space–time fields are now written as functions of $(\boldsymbol{x}, \tilde{t})$, and all temporal derivatives are taken with respect to the pseudo-time $\tilde{t}$.

Let W_0 be an orthonormal basis for the subspace V_0^Q. The component expansion of Eq. (33) is

$$\int_Q \{-\dot{w}_{i,j}\sigma_h^{ij} + \rho\ddot{w}_i\dot{u}_h^i + \rho\dot{w}_i b^i\}\mathrm{d}\mathbf{V} + \int_{\partial Q} \{\dot{w}_i(\sigma_h^{ij})^* n_j - \dot{w}_i(p_h^i)^* n_{\tilde{t}} - [\![E_{ij}]\!]\hat{\sigma}^{ij} n_{\tilde{t}} + [\![\dot{u}_i]\!]\hat{\sigma}^{ij} n_j\}\mathrm{d}\mathbf{S}$$

$$+ \int_{\partial Q^{\mathrm{ti}}} (w_0)_i [\![u^i]\!] n_{\tilde{t}}\,\mathrm{d}\mathbf{S} = 0 \quad \forall \mathbf{w} \in V^Q, \tag{A.1}$$

in which

$$\mathbf{w}_0 = \sum_{\mathbf{v} \in W_0} \left\{ -\int_{\partial Q^{\mathrm{ti}}} w_i v^i n_{\tilde{t}}\,\mathrm{d}\mathbf{S} \right\}\mathbf{v}, \tag{A.2}$$

$[\![f]\!] := f^* - f$, $\mathbf{n} = n_i \mathbf{e}^i + n_{\tilde{t}}\tilde{\mathbf{e}}^i$ is the outward space–time unit normal vector field on ∂Q in which $\tilde{\mathbf{e}}^i$ is the orthonormal basis vector in the pseudo-time direction, and $\mathrm{d}\mathbf{S}$ and $\mathrm{d}\mathbf{V}$ are space–time surface and volume differentials in $\mathbb{E}^{d+1}$. The definitions of target values $(\cdot)^*$ are given in (29) and (30) and in Appendix B.

Appendix B. Definitions of Godunov values

The following subsections present expressions for the Godunov values of stress and velocity. The Godunov strains are obtained by applying the inverse constitutive relation to the Godunov stresses, and the Godunov momentum densities are obtained by applying the forward constitutive relation to the Godunov velocities.

B.1. Godunov values for solutions on $\mathbb{E}^1 \times \mathbb{R}$

Let $c = \sqrt{E/\rho}$ denote the elastic wave speed in which E denotes Young's modulus. We drop all subscripts in this section since there is only one spatial direction. Consider a causal patch in $\mathbb{E}^1 \times \mathbb{R}$, as shown in Fig. B.1(a). The Godunov values of the mechanical fields on the noncausal interface $\Gamma_{\alpha\beta}$ are functions of the fields on the adjacent elements, Q_α and Q_β:

$$\sigma^G = \frac{1}{2}(\sigma^\alpha + \sigma^\beta) + \frac{E}{2c}(\dot{u}^\beta - \dot{u}^\alpha), \tag{B.1a}$$

$$\dot{u}^G = \frac{1}{2}(\dot{u}^\alpha + \dot{u}^\beta) + \frac{c}{2E}(\sigma^\beta - \sigma^\alpha). \tag{B.1b}$$

B.2. Godunov values for solutions on $\mathbb{E}^2 \times \mathbb{R}$

Consider a causal patch in $\mathbb{E}^2 \times \mathbb{R}$, as shown in Fig. B.2. We find the Godunov values by solving a one-dimensional Riemann problem in the spatial direction **n** that is normal to the noncausal interface $\Gamma_{\alpha\beta}$, as shown in Fig. B.3(a). For this purpose, it is convenient to introduce local spatial coordinates ξ_1 and ξ_2, such that ξ_1 points in the same direction as **n**, and ξ_2 is tangent to $\Gamma_{\alpha\beta}$ and forms a right-hand system with the time coordinate t (Fig. B.3(a)).

Let μ and λ denote the Lamè parameters. We define

$$\hat{\lambda} = \begin{cases} \lambda & \text{for plane strain,} \\ \dfrac{2\mu\lambda}{\lambda + 2\mu} & \text{for plane stress,} \end{cases} \tag{B.2a}$$

$$\hat{c}_p = \sqrt{\frac{\hat{\lambda} + 2\mu}{\rho}}, \tag{B.2b}$$

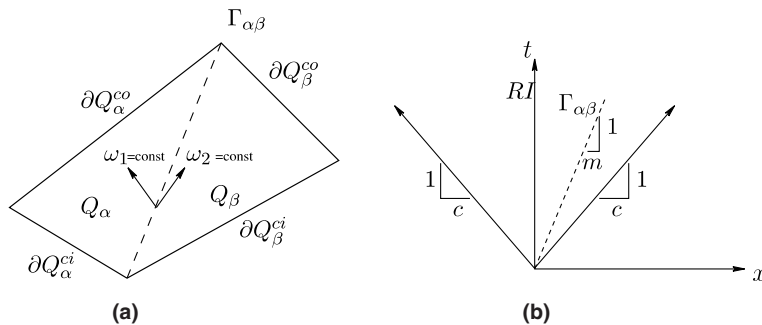$$c_s = \sqrt{\frac{\mu}{\rho}}. \tag{B.2c}$$

Fig. B.1. Regions for a noncausal interface in $\mathbb{E}^1 \times \mathbb{R}$: (a) inclined interface, (b) regions for $\Gamma_{\alpha\beta}$.
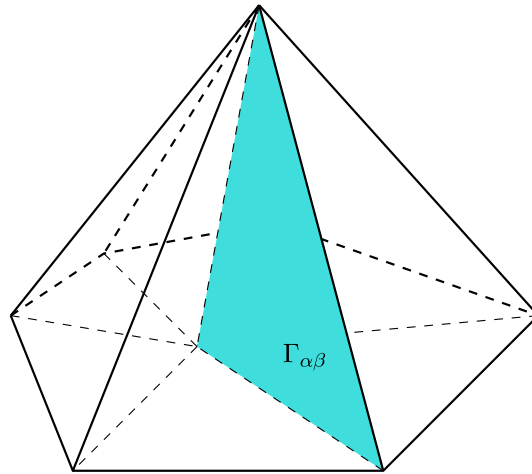
Fig. B.2. Causal patch in $\mathbb{E}^2 \times \mathbb{R}$ with noncausal interface $\Gamma_{\alpha\beta}$.

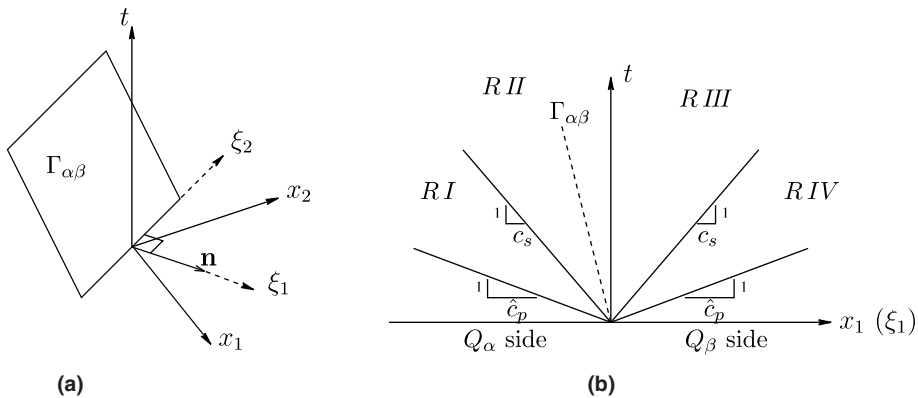**(a)**   **(b)**

Fig. B.3. Coordinates and inclination of a noncausal interface in $\mathbb{E}^2 \times \mathbb{R}$: (a) local coordinates on noncausal interface $\Gamma_{\alpha\beta}$, (b) regions (*RI–RIV*) for classifying the inclination of the interface $\Gamma_{\alpha\beta}$.

Depending on which region contains the inclined manifold $\Gamma_{\alpha\beta}$ (see Fig. B.3), the components of the Godunov values with respect to the local spatial coordinate frame (see Fig. B.3(a)) are given by

$$(\sigma^{11})^G = \frac{1}{2}\{(\sigma^{11})^\alpha + (\sigma^{11})^\beta\} + \frac{\rho \hat{c}_p}{2}[\dot{u}_1] \qquad \text{All regions,} \tag{B.3a}$$

$$(\sigma^{22})^\alpha = \begin{cases} (\sigma^{22})^\alpha + \dfrac{\hat{\lambda}}{2(\hat{\lambda}+2\mu)}[\sigma^{11}] + \dfrac{\hat{\lambda}}{2\hat{c}_p}[\dot{u}_1] & \text{Regions I and II,} \\[3mm] (\sigma^{22})^\beta - \dfrac{\hat{\lambda}}{2(\hat{\lambda}+2\mu)}[\sigma^{11}] + \dfrac{\hat{\lambda}}{2\hat{c}_p}[\dot{u}_1] & \text{Regions III and IV,} \end{cases} \tag{B.3b}$$

$$(\sigma^{12})^G = \begin{cases} (\sigma^{12})^\alpha & \text{Region I,} \\[2mm] \dfrac{1}{2}\{(\sigma^{12})^\alpha + (\sigma^{12})^\beta\} + \dfrac{\rho c_s}{2}[\dot{u}_2] & \text{Regions II and III,} \\[2mm] (\sigma^{12})^\beta & \text{Region IV,} \end{cases} \tag{B.3c}$$

$$\dot{u}_1^G = \frac{1}{2}(\dot{u}_1^\alpha + \dot{u}_1^\beta) + \frac{1}{2\rho\hat{c}_p}[\sigma^{11}] \qquad \text{All regions,} \tag{B.3d}$$

$$\dot{u}_2^G = \begin{cases} \dot{u}_2^\alpha & \text{Region I,} \\ \frac{1}{2}(\dot{u}_2^\alpha + \dot{u}_2^\beta) + \frac{1}{2\rho c_s}[\sigma^{12}] & \text{Regions II and III,} \\ \dot{u}_2^\beta & \text{Region IV,} \end{cases} \tag{B.3e}$$

in which

$$[f] = f^\beta - f^\alpha. \tag{B.4}$$

References

[1] T.J.R. Hughes, The Finite Element Method: Linear Static and Dynamic Finite Element Analysis, Dover Publications, 2000.
[2] Z. Ge, J.E. Marsden, Lie–Poisson Hamilton–Jacobi theory and Lie–Poisson integrators, Phys. Lett. A 133 (1988) 134–139.
[3] P. Betsch, P. Steinmann, Conservation properties of a time FE method. Part I: time-stepping schemes for *n*-body problems, Int. J. Numer. Methods Engrg. 49 (2000) 599–638.
[4] P. Betsch, P. Steinmann, Conservation properties of a time FE method. Part II: time-stepping schemes for non-linear elastodynamics, Int. J. Numer. Methods Engrg. 50 (2001) 1931–1955.
[5] E. Graham, G. Jelenić, A general framework for conservative single-step time-integration schemes for higher-order accuracy for a central-force system, Comput. Methods Appl. Mech. Engrg. 192 (2003) 3585–3618.
[6] C. Kane, J.E. Marsden, M. Ortiz, M. West, Variational integrators and the new-mark algorithm for conservative and dissipative mechanical systems, Int. J. Numer. Methods Engrg. 49 (2000) 1295–1325.
[7] A. Lew, J.E. Marsden, M. Ortiz, M. West, Asyncronous variational integrators, Arch. Rat. Mech. Anal. 167 (2003) 85–146.
[8] A. Lew, J.E. Marsden, M. Ortiz, M. West, Variational time integrators, Int. J. Numer. Methods Engrg. 60 (2004) 153–212.
[9] T.J.R. Hughes, G.M. Hulbert, Space-time finite element methods for elastodynamics: Formulations and error estimates, Comput. Methods Appl. Mech. Engrg. 66 (1988) 339–363.
[10] G.M. Hulbert, T.R.J. Hughes, Space-time finite element methods for second order hyperbolic equations, Comput. Methods Appl. Mech. Engrg. 84 (1990) 327–347.
[11] X.D. Li, N.E. Wiberg, Structural dynamic analysis by a time-discontinuous Galerkin finite element method, Int. J. Numer. Methods Engrg. 39 (12) (1996) 2131–2152.
[12] X.D. Li, N.E. Wiberg, Implementation and adaptivity of a space–time finite element method for structural dynamics, Comput. Methods Appl. Mech. Engrg. 156 (1998) 211–229.
[13] D.A. French, A space–time finite element method for the wave equation, Comput. Methods Appl. Mech. Engrg. 107 (1993) 145–157.
[14] C. Johnson, Discontinuous Galerkin finite element methods for the wave equation, Comput. Methods Appl. Mech. Engrg. 107 (1993) 117–129.
[15] I. Romero, On the stability and convergence of fully discrete solutions in linear elastodynamics, Comput. Methods Appl. Mech. Engrg. 191 (2002) 3857–3882.
[16] G.R. Richter, An explicit finite element method for the wave equation, Appl. Numer. Math. 16 (1994) 65–80.
[17] R.S. Falk, G.R. Richter, Explicit finite element methods for symmetric hyperbolic equations, SIAM J. Numer. Anal. 36 (1999) 935–952.
[18] L. Yin, A. Acharia, N. Sobh, R.B. Haber, D.A. Tortorelli, A space–time discontinuous Galerkin method for elastodynamics analysis, in: B. Cockburn, G. Karriadakis, C.W. Shu (Eds.), Discontinuous Galerkin Methods: Theory, Computation and Applications, Springer Verlag, 2000, pp. 459–464.
[19] L. Yin, A new space–time discontinuous Galerkin finite element method for elastodynamics analysis, Ph.D. thesis, Department of Theoretical and Applied Mechanics, University of Illinois, 2002.
[20] J. Palaniappan, R.B. Haber, R.L. Jerrard, A space–time discontinuous Galerkin method for scalar conservation laws, Comput. Methods Appl. Mech. Engrg. 193 (2004) 3607–3631.
[21] B. Petracovici, Analysis of a space–time discontinuous Galerkin method for elastodynamics, Ph.D. thesis, Department of Mathematics, University of Illinois, 2004.
[22] J. Erickson, D. Guoy, J. Sullivan, A. Üngör, Building space–time meshes over arbitrary spatial domains, in: Proceedings of the 11th International Meshing Roundtable, Sandia National Laboratories, 2002, pp. 391–402.
[23] R. Abedi, S. Chung, J. Erickson, Y. Fan, M. Garland, D. Guoy, R.B. Haber, J. Sullivan, Y. Zhou, Space-time meshing with adaptive refinement and coarsening, in: Proceedings 20th Annual ACM Symposium on Computational Geometry, Brooklyn, NY, 2004, pp. 300–309.

[24] R.L. Bishop, S.I. Goldberg, Tensor Analysis on Manifolds, Prentice Hall, Englewood Cliffs, New Jersey, 1980, reprinted By Dover, 1980.

[25] W.H. Fleming, Functions of Several Variables, Addison-Wesley, Reading, MA, 1964.

[26] M. Spivak, Calculus on Manifolds, W.A. Benjamin, New York, 1965.

[27] M.E. Gurtin, The Linear Theory of Elasticity, Handbuch der Physik, vol. Va/2, Springer Verlag, Berlin, 1972.

[28] Y. Zhou, M. Garland, R.B. Haber, Pixel-exact rendering of space–time finite element solutions, in: Proceedings of IEEE Visualization 2004, 2004, pp. 425–432.

[29] H.L. Atkins, C.W. Shu, Quadrature-free implementation of discontinuous Galerkin method for hyperbolic equations, AIAA J. 36 (1998) 775–782.